Gold endowment and unloading along pathway for giant gold mineralization: Insights from spatiotemporal variations of in-situ pyrite geochemistry and gold fineness from the Jiaodong gold deposits, north China Craton

Ting-Guang Lan [a,b,*], Hong Wang [a,b], Hong-Rui Fan [b,c], Thomas Ulrich [d], Huan-Long Hu [a], You-Wei Chen [a], Lei Shu [e]

[a] State Key Laboratory of Ore Deposit Geochemistry, Institute of Geochemistry, Chinese Academy of Sciences, Guiyang 550081, China
[b] College of Earth Sciences, University of Chinese Academy of Sciences, Beijing 100049, China
[c] Key Laboratory of Mineral Resources, Institute of Geology and Geophysics, Chinese Academy of Sciences, Beijing 100029, China
[d] Institute for Geosciences, Aarhus University, Aarhus 8000, Denmark
[e] MNR Key Laboratory of Gold Mineralization Processes and Resources Utilization, Shandong Institute of Geological Sciences, Jinan 250013, China

ARTICLE INFO

ABSTRACT

Over 5000 tonnes of gold were accumulated in the Jiaodong Peninsula at the early Cretaceous, the sources and critical ore-forming processes of which are still controversial. Here, we conducted comprehensive in-situ textural, elemental and isotopic analyses on pyrite and gold grains from the different mineralization styles, hydrothermal stages and depths for three representative gold deposits (Linglong, Xiadian and Jiangjiayao) from the northwestern Jiaodong Peninsula, with the aim to exactly constrain the sources and ore-forming processes. Three groups of $\delta^{34}S_{pyrite}$ were identified in the studied deposits, of which the Group 1 shows stable and low $\delta^{34}S$ (4.8–7.6‰) throughout the hydrothermal evolution while the Group 2 has elevated $\delta^{34}S$ (6.0–12.8‰) coupled with increasing As and Au concentrations. The Group 3 shows moderate $\delta^{34}S$ (5.2–9.8‰) accompanied by high Al and Si concentrations. The Group 1 suggests a low-$\delta^{34}S$ primary auriferous fluid derived from a mantle-related source, whereas the Group 2 indicates the primary auriferous fluid leaching additional S, As and Au from the Precambrian metasedimentary rocks along pathway. The Group 3 is petrographically coupled with numerous silicate inclusions, indicating enhanced fluid-rock interaction between the auriferous fluids and the granitic wallrcoks. Gold fineness decreases from the early to the late hydrothermal stages, combined with increasing deposition of polymetallic sulfides, suggesting an increase of pH resulting in efficient Au deposition. Gold fineness and Bi concentrations in pyrite decrease with shallowing, suggesting that cooling affected Au deposition as well. Bismuth-Te-S minerals were identified in the deep depths, combined with the well correlated Bi and Ag, implying that Bi-Te complexes might play a role in transporting Au and Ag at high-temperature conditions. The above results corroborate that multiple sources and ore-forming processes were responsible for the giant gold mineralization, of which the gold endowment from Precambrian wallrocks needs to be further concerned.

© 2023 International Association for Gondwana Research. Published by Elsevier B.V. All rights reserved.

1. Introduction

It has been argued whether metal-rich sources or enhanced ore-forming processes are required or not in the formation of giant gold deposits (Simmons and Brown, 2006; Wilkinson et al., 2009; Richards, 2013; Groves et al., 2016; Moncada et al., 2019). Because multistage fluids or long-duration ore-forming processes commonly occur in giant gold deposits (Moncada et al., 2019), the Au budget might change over time and space, leading to the confusions of which factors controlled the mineralization. To better constrain the sources and mineralization mechanisms, investigating the temporal and spatial variations of the ore-forming processes is necessary.

The Jiaodong Peninsula, China is one of the largest gold provinces in the world, hosting > 150 gold deposits and > 5000 tonnes of gold

within an area < 30000 km^2 (Goldfarb and Santosh, 2014; Deng et al., 2020b). The gold deposits formed focusedly at 120 ± 2 Ma (Zhang et al., 2020), being 10–40 Ma younger than their host granitoids or 1.8 Ga later than the metamorphism of their host metamorphic rocks. They have simple mineral assemblages of Au-bearing quartz + sulfide and uniform ore-forming fluids characterized by high CO_2 contents (10–20 mol%), low salinities (commonly < 10 wt% $NaCl_{eqv.}$) and moderate to low homogenization temperatures (mainly 200–350 °C) (Qiu et al., 2002; Fan et al., 2007; Li et al., 2015). The salinities and homogenization temperatures of fluid inclusions do not change too much between different deposits or within the depth range of 0 to −4000 m (Wen et al., 2015, 2016; Guo et al., 2017; Liu et al., 2018). Neither magmatic nor metamorphic events have been directly linked to these deposits (Goldfarb and Santosh, 2014). It is thus puzzled how such huge amounts of gold were derived and deposited within a narrow area during a short time interval. Many genetic models, such as crustal reworking (e.g., Wang et al., 1989; Chen et al., 2005; Yan et al., 2014), mantle melting/devolatilization (e.g., Deng et al., 2020b; Wang et al., 2020; Xiong et al., 2021), and oceanic slab dehydration (e.g., Goldfarb and Santosh, 2014; Groves and Santosh, 2016; Zhu and Sun, 2021), have been proposed for the genesis of these deposits. However, because the isotopic compositions (e.g., C-O-S-Sr-Nd-Pb-He-Ar) of ores commonly show mixed features between the crustal and mantle end-members (Mao et al., 2008; Li and Santosh, 2014; Li et al., 2015; Deng et al., 2020a, 2020b), the above models cannot fully explain the origin of the ore-forming materials.

Pyrite is the dominant Au-hosting mineral in the Jiaodong gold deposits. With the developments of laser ablation-(multi-collector)-inductively coupled plasma-mass spectrometry (LA-(MC)-ICP-MS) technique in recent years, the in-situ elemental and isotopic compositions of pyrite can be well analyzed and have been widely used to trace the origin, transportation and deposition of Au for the Jiaodong gold deposits (e.g., Mills et al., 2015; Yang et al., 2016a; Li et al., 2018; Fan et al., 2021; Li et al., 2021; Peng et al., 2021; Yuan et al., 2021). However, these studied mainly focused on a single deposit, leaving the regional or spatiotemporal evolution of the ore-forming processes being poorly constrained. Electrum is ubiquitous in the Jiaodong gold deposits. The fineness of electrum is a function of temperature, pH, oxygen fugacity, Au/Ag ratio and Cl and S concentrations (Gammons and Williams-Jones, 1995; Pal'yanova, 2008; Liang and Hoshino, 2015), which can reflect the physicochemical conditions of the fluids. Therefore, in this contribution, using the in-situ analytical methods of scanning electron microscope (SEM), focused ion beam-transmission electron microscope (FIB-TEM) and LA-(MC)-ICP-MS, integrated textural, elemental and isotopic analyses of pyrite from different mineralization styles (lode-style and disseminated and stockwork-style), early to late hydrothermal stages (Au-barren quartz ± pyrite, Au-bearing quartz + pyrite and quartz + polymetallic sulfide stages) and deep to shallow depths (altitudes of −10 to −1600 m) were conducted for three representative gold deposits (Linglong, Xiadian and Jiangjiayao gold deposits) in one fault belt (Zhaoyuan-Pingdu fault belt) from the northwestern Jiaodong Peninsula. Electrum grains were also analyzed by FIB-TEM and electron probe microanalyzer (EPMA) to investigate their micro-textures and gold fineness. The above analyses allow us to fully assess how the Au was sourced, transported and deposited over time and space and thus yield insights into the generation of the giant gold mineralization.

2. Regional geology

The Jiaodong Peninsula is located at the eastern margin of the North China Craton (NCC), eastern China, which is bordered to the north, south and east by the Bohai and Yellow seas and to the west by the Tan-Lu fault belt, respectively (Fig. 1). It is mainly composed of Precambrian basement and Mesozoic granitoids, volcanics and ultra-high-pressure (UHP) metamorphic rocks. The Precambrian basement rocks mostly occur in the northwestern Jiaodong Peninsula, which include the Mesoarchean to Neoarchean (2.9–2.7 Ga) tonalite-trondhjemite-granodiorite gneisses, biotite-plagioclase gneisses and amphibolites and the Paleoproterozoic (2.3–2.0 Ga) sillimanite-biotite-quartz schists, biotite gneisses, amphibolites, marbles and graphite-bearing rocks (Wan et al., 2006; Jahn et al., 2008). These rocks were suffered amphibolite to granulite facies metamorphism at ∼ 2.5 Ga and greenschist to granulite facies metamorphism at 1.9–1.8 Ga, respectively (Wan et al., 2006; Jahn et al., 2008). Minor Neoproterozoic unmetamorphosed or slightly metamorphosed slates, phyllites and limestones occur in the northeastern Jiaodong Peninsula. Mesozoic granitoids are widespread in the whole Jiaodong Peninsula, including the late Triassic (240–225 Ma) alkaline complex, late Jurassic (160–150 Ma) granites, and early Cretaceous (130–113 Ma) granodiorites, (alkaline) granites and monzonites (Yang et al., 2005; Goss et al., 2010; Yang et al., 2012). Early Cretaceous (118–93 Ma) basaltic to rhyolitic volcanics occur in the Jiaolai Basin of the central-southwestern Jiaodong Peninsula (Ling et al., 2007). Mafic to felsic dykes emplaced at the early Cretaceous (131–110 Ma) are also widespread (Li et al., 2016; Deng et al., 2017), especially in the goldfields. Late Triassic UHP rocks occur in the southeastern Jiaodong Peninsula, which have been considered to be the continental margin rocks of the South China Block that were deeply subducted (>80 km) underneath the NCC and underwent UHP metamorphism during 240–225 Ma (Wu and Zheng, 2013). The Jiaodong Peninsula was suffered intense extension during the early Cretaceous, forming a series of NE- to NNE-trending faults and numerous fault-controlled gold deposits (Deng et al., 2019; Zhu et al., 2021). After the Mesozoic, the Jiaodong Peninsula kept relatively stable, within which only minor basalts occurred during the Cenozoic.

3. Deposit geology

The gold deposits in the Jiaodong Peninsula are mainly distributed along the NE- to NNE-trending faults, which have been classified into the Zhaoyuan-Laizhou, Penglai-Qixia and Muping-Rushan gold belts from the west to the east (Fig. 1). The gold deposits are mainly hosted by Mesozoic granitoids with some by Precambrian metamorphic rocks. Gold mineralization occurs either as Au-bearing quartz + sulfide lodes or as disseminations and stockworks in altered rocks, which are referred to Linglong-type and Jiaojia-type mineralization, respectively (Qiu et al., 2002). The two mineralization styles cannot be distinguished in age, wall-rock, alteration type and fluid inclusion (Li et al., 2015; Wen et al., 2015; Guo et al., 2017), but differ in structural setting, where the Linglong-type mainly occurs in the lower-order steep-dipping (e.g., >60°) fractures distal to the regional-scale main faults while the Jiaojia-type occurs in the less steep (e.g., <45°) fractures close to the major faults (Qiu et al., 2002; Li et al., 2015). Hydrothermal alteration is ubiquitous in all the deposits, which mainly includes K-feldspathization, sericitization, silicification and sulfidation. The alteration types are often zoned inward from the wallrocks to the orebodies with the sequence of K-feldspathization → silicification/sericitization → sulfidation. Four major hydrothermal stages have been identified in the Jiaodong gold deposits (Qiu et al., 2002): (I) pre-mineralization quartz ± K-feldspar ± pyrite stage, (II) Au-bearing quartz + pyrite stage, (III) Au-bearing quartz + polymetallic sulfide (e.g., pyrite, pyrrhotite, chalcopyrite, galena and sphalerite) stage and (IV) post-mineralization
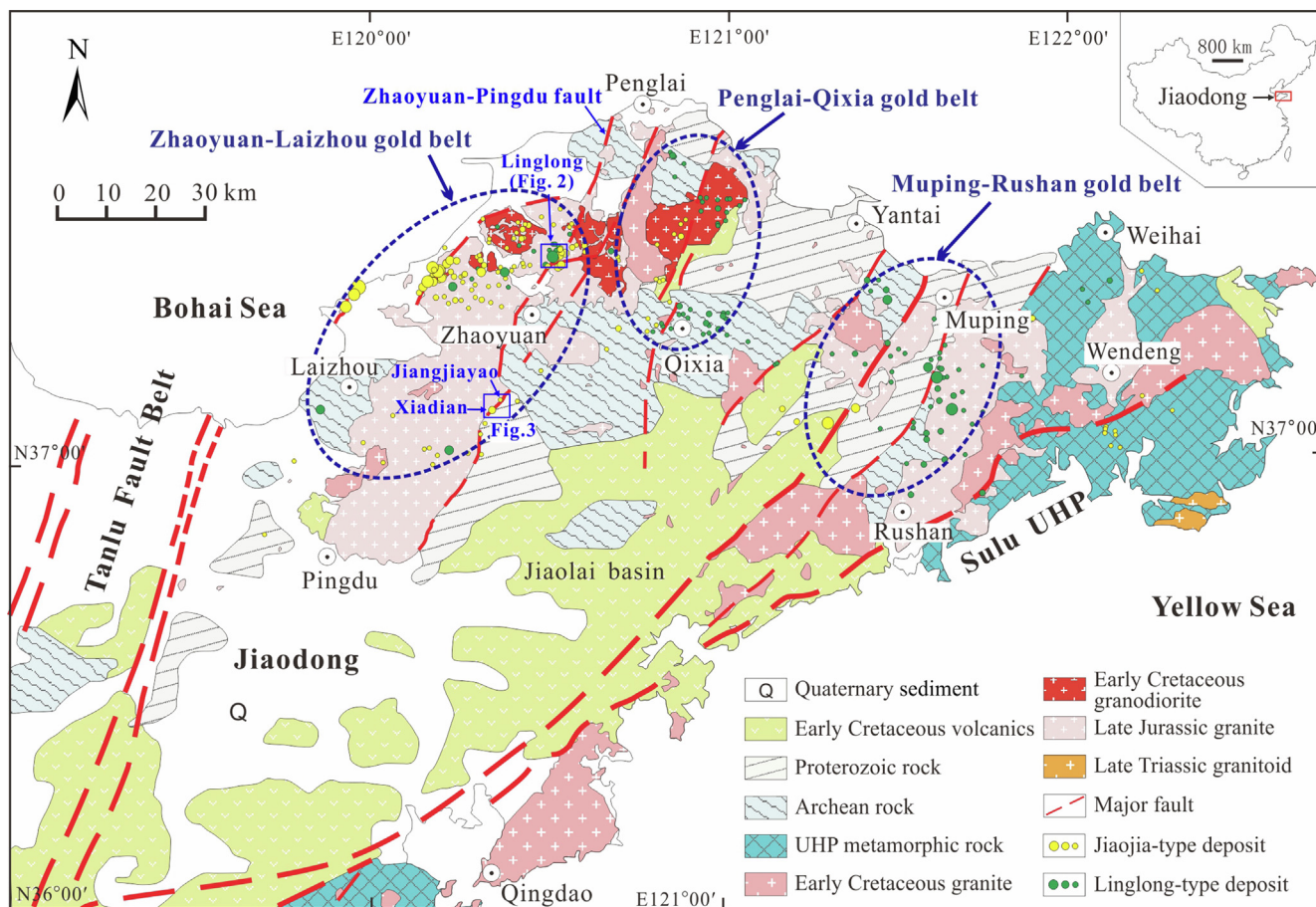
Fig. 1. Geological map of the Jiaodong Peninsula and the distribution of gold deposits (modified after Wen et al., 2016).

quartz + carbonate stage. The stage II and III are the ore-forming stages, of which the stage II is dominant.

The Zhaoyuan-Pingdu fault is one of the major Au-hosting faults in the Zhaoyuan-Laizhou gold belt (Fig. 1). It not only hosts over 600 tonnes of Au, but also contains different mineralization types. The Linglong-type mineralization typically occurs at the northern section of the Zhaoyuan-Pingdu fault, which is represented by the world-class Linglong gold deposit (broadly called the Linglong goldfield, with predicted Au resources > 500 tonnes). The goldfield comprises numerous NE- to NNE-trending ore veins (>200) that have been divided into different ore districts (e.g., Xishan, Dong-shan, Dakaitou, Jiuqu, Shuangding, Oujiakuang, Taishang, Dongfeng and Luoshan districts, Fig. 2). Ore veins are dominantly hosted by late Jurassic (~160 Ma) granites with less by early Cretaceous (~130 Ma) granodiorites. They occur along secondary faults of the Zhaoyuan-Pingdu fault and are roughly parallel (Fig. 2). The veins are commonly 0.5–10 m in width, 100–5500 m in length and + 600 to −1000 m in altitude, which strike NE-NEE-NNE and dip NW 50°-80°. Gold grades vary widely from several to hundreds of g/t, but are mainly 5–8 g/t. The Jiaojia-type mineralization typically occurs at the southern section of the Zhaoyuan-Pingdu fault and is represented by the Xiadian and Jiangjiayao gold deposits (Fig. 1). The two deposits are located about 20–25 km away from the Linglong gold deposit. They show consistent geological features with each other, hosting proven Au resources of ~ 83 and ~ 26 ton-nes, respectively. The gold mineralizaion mainly occurs at the con-tacts between the late Archean metamorphic rocks (hangingwall) and the late Jurassic granites (footwall) along the regional Zhaoyuan-Pingdu fault (Fig. 3a). From the hangingwall to the foot-

wall, the rocks commonly show zoning of potassic-sericitic meta-morphic rocks → fault gouges → cataclastic beresites/ beresitization granites → potassic-sericitic granites (Fig. 3b-c). Beresites or beresitization granites are commonly the orebodies, in which both disseminated sulfides and quartz + sulfide stock-works occur. Hydrothermal alteration types are similar to those in the Linglong gold deposit, but show stronger superposition by different hydrothermal stages. In the Xiadian deposit, the orebod-ies are commonly 0.7–10 m in width, 90–510 m in length and + 160 to − 600 m in altitude, which strike NE 28–48° and dip SE 42–50°. Gold grades vary from 1 to 55 g/t with an average grade of 4–9 g/t. In the Jiangjiayao deposit, the orebodies are 1– 8 m in width, 20–300 m in length and + 160 to − 350 m in altitude, and strike NE 40–50° and dip SE 47–51°. Gold grades vary from 1 to 24 g/t with an average grade of 4–5 g/t.

The coexistence of distinct mineralization types in one fault belt facilitates the comparisons of how the Au was transported and deposited along pathway. Representative samples of the Linglong-type and Jiaojia-type mineralization were thus collected.

4. Sampling and analytical methods

For the Linglong-type mineralization, pyrite samples from the early to the late hydrothermal stages (I, II and III) were systemati-cally collected from the Linglong gold deposit to constrain the tem-poral evolution of the gold mineralization. Twenty-five samples were collected from the mining tunnels of the Xishan ore district at the depths (altitude) of −10 to −50 m (Fig. 2). Strong hydrother-
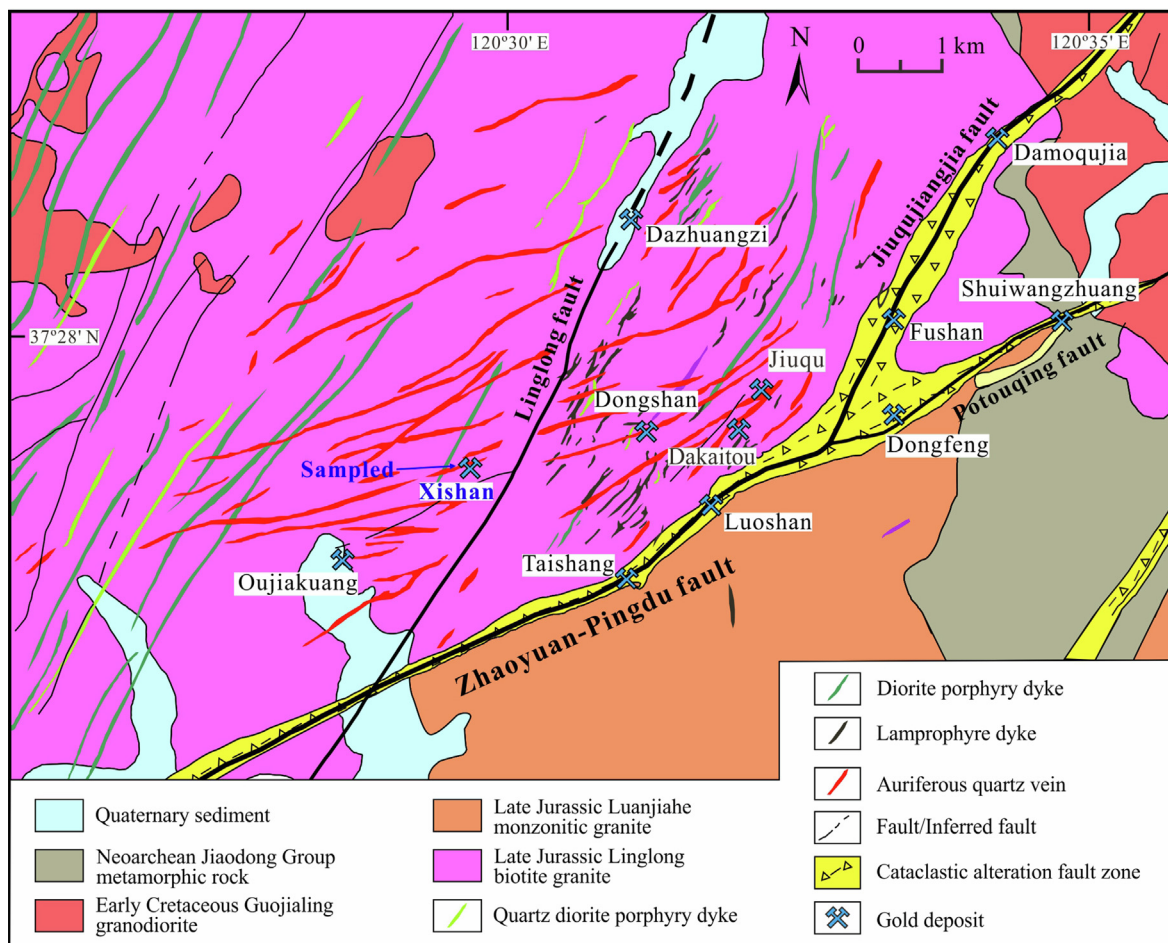
Fig. 2. Geological map of the Linglong goldfield (modified after Yang et al., 2016b).

mal superimposition occurred in the Jiaojia-type mineralization, leading to the difficulties in identifying the different hydrothermal stages. Nonetheless, the Au-bearing quartz + pyrite veinlets from the hydrothermal stage II can be clearly identified and are also widespread in the Xiadian and Jiangjiayao deposits. Because these veinlets can represent the major ore-forming stage with least superimposition or contamination, they were selected for studying. Twenty-six samples from the Xiadian deposit were collected from the mining tunnels at the depths of −450 to −652 m. Thirty-four samples from the Jiangjiaoyao deposit were collected from the drill hole (ZK5) at the depths of −1500 to −1600 m. These samples from different depths facilitate to study the vertical variations of the gold mineralization. Samples were made into doubly-polished thin sections for petrographic observations and SEM, EPMA, FIB-TEM and LA-(MC)-ICP-MS analyses. To avoid mixed or contaminated elemental and isotopic compositions, detailed back-scattered electron (BSE) imaging of almost all the analyzed spots was conducted before the EPMA, FIB-TEM and LA-(MC)-ICP-MS analyses. The detailed sample information and analytical items are listed in Table 1.

4.1. SEM and EPMA analyses

Back-scattered electron (BSE) imaging was conducted to identify the internal textures and generations of pyrite using a JSM-7800F SEM at the State Key Laboratory of Ore Deposit Geochemistry (SKLODG), Institute of Geochemistry, Chinese Academy

of Sciences (IGCAS), Guiyang, China. The working conditions were 20 kV accelerating voltage and 10nA beam current.

Major element analyses of sulfides and visible gold grains were also conducted at the SKLODG using a JXA8530F-plus EPMA. Calibrations were carried out using the standards provided by the company of Structure Probe, Inc. (SPI Supplies). Matrix effects were corrected using the ZAF software provided by the JEOL. The working conditions were 25 kV accelerating voltage and 10nA beam current.

4.2. FIB-TEM analysis

High-resolution examinations of pyrite and gold textures were conducted by FIB-TEM. Thin lamella liftouts of samples were accomplished on a FEI Scios DualBeam FIB equiped with a SEM at the Center for Lunar and Planetary Sciences (CLPS), IGCAS. The above samples were moved to a Tecnai G^2 F20 S-TWIN TEM for nanoscale imaging at the State Key Laboratory of Environmental Geochemistry (SKLEG), IGCAS. The TEM operation conditions were 200 kV accelerating voltage and 1nA beam current.

4.3. LA-ICP-MS elemental analysis (spot analysis and mapping)

Quantitative major and trace element analyses of pyrite were conducted by LA-ICP-MS at the SKLODG, IGCAS. Laser sampling was performed using a RESOlution S155-LR ArF 193 nm laser ablation system. A two-volume sample cell is equipped in this system
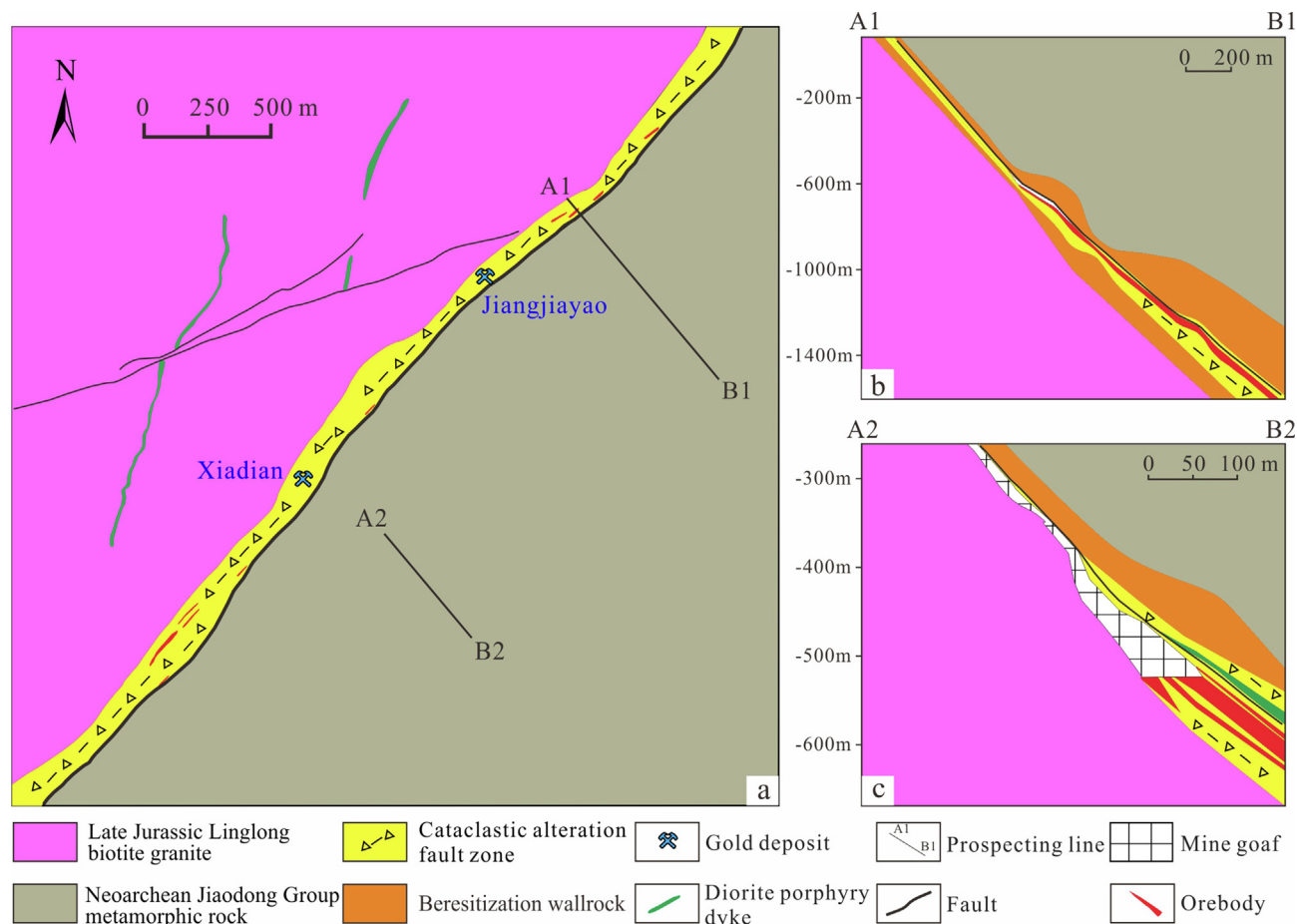
Fig. 3. Geological maps of the Jiangjiayao and Xiadian gold deposits (modified after Chai et al., 2017).

and mixtures of He (350 ml/min) and Ar (900 ml/min) were applied as the carrier gas. Laser spot size of 26 μm, repetition of 6 Hz and fluence of 3 J/cm^2 were used during the analyses. Each analysis incorporated a background acquisition of approximately 30 s followed by 60 s of data acquisition from the sample. An Agilent 7700x ICP-MS was used to acquire the ion-signal intensities. Quantitative calibrations referred to the methods of Danyushevsky et al. (2011) and Yuan et al. (2012), in which the sulfide standard STDGL2b2 and glass standard GSD-1G were used as external standards while the stoichiometric Fe contents were used as internal standard. The standards of MASS-1 and GSE-1G were also analyzed to monitor the accuracy, which show that most of the analyzed elements have the accuracies better than 10%. The preferred elemental concentrations for the USGS reference glasses (GSD-1G and GSE-1G) are from the GeoReM database (https://geo-rem.mpch-mainz.gwdg.de/) while the MASS-1 and STDGL2b2 are from Wilson et al. (2002) and Danyushevsky et al. (2011), respectively. The data processing was performed using the *Iolite* software (Paton et al., 2011).

Element-distribution mapping of pyrite was also conducted. Pre-selected areas were ablated by defining a number of equally spaced lines. The spot size, spacing between individual lines and scanning speed were typically designed to ensure the image resolution with appropriate acquisition time (Ulrich et al., 2009). In this study, lines were ablated using the laser spot size of 10 μm, repetition rate of 10 Hz, fluence of 3 J/cm^2 and scanning speed of 7 μm/ s. After setting up the ablation parameters, the analyses were fully automated and controlled by the laser software of *GeoStar* and the

mass spectrometer. Processing and imaging of the data were done using the *Iolite* software (Paton et al., 2011). The STDGL2b2 and GSD-1G were used as calibration standards.

4.4. LA-MC-ICP-MS sulfur isotopic analysis

In-situ sulfur isotopic analysis of pyrite ($\delta^{34}S_{V-CDT}$) was performed on a Nu Plasma III MC-ICP-MS attached to a RESOlution S155-LR ArF 193 nm laser ablation system at the SKLODG. To collect the coupled elemental and isotopic compositions, isotopic measurements were conducted on or near the spots that were analyzed for elements. Laser spot size of 48 μm, repetition of 5 Hz and fluence of 3 J/cm^2 were used during the analyses. The ablated products were carried by the mixed He (350 ml/min), Ar (800 ml/min) and N$_2$ (2 ml/min) gases to the MC-ICP-MS. Each analysis incorporated a background acquisition of approximately 20 s (gas blank) followed by 40 s of data acquisition from the sample and 40 s of washout. All analyses followed standard-sample bracketing procedure, in which an external standard (a pressed pyrite powder tablet, PSPT-2) was repeatedly measured every five unknown samples for mass bias correction (Bao et al., 2017). Two in-house pyrite standards (natural crystals, SB-1 from Shangbao W-Sn deposit and HYC-1 from Huayangchuan Nb-U-REE deposit, China) were analyzed twice every five unknown samples to monitor the accuracy. The measured $\delta^{34}S_{V-CDT}$ values are 16.7 ± 0.7‰ (n = 52, 2SD) for SB-1 and −5.5 ± 0.5‰ for HYC-1 (n = 52, 2SD), respectively, which are well consistent with the recommended values (16.6‰ for SB-1 and

Table 1
Locations and descriptions of the samples selected for pyrite and gold studies.

Location	Altitude (m)	Hydrothermal stage	Description	LA-ICP-MS elemental analysis of pyrite	LA-MC-ICP-MS sulfur isotopic analysis of pyrite	EPMA analysis of visible gold	SEM analysis of pyrite and gold	LA-ICP-MS elemental mapping of pyrite	FIB-TEM analysis of pyrite and gold
Linglong deposit	−50	Stage I	Euhedral Py grains disseminated in altered granite	17LL04	17LL04		17LL04	17LL04	
	−50	Stage IIa	Gold-bearing Qz + Py veins	17LL01, 17LL05-2, 17LL09	17LL01, 17LL05-2, 17LL09	17LL05-2	17LL01, 17LL05-2, 17LL09	17LL09	
	−10	Stage IIb	Gold-bearing Qz + Py veins	17LL07	17LL07	17LL07	17LL07	17LL07	17LL07
	−10	Stage III	Gold-bearing Qz + polymetallic sulfide veins			17LL10-1, 17LL10-2	17LL10-1, 17LL10-2	17LL10-2	
	−10	Stage III	Gold-bearing Qz + polymetallic sulfide veins	17LL13-1, 17LL13-2	17LL13-1, 17LL13-2	17LL13-2	17LL13-1, 17LL13-2	17LL13-1	
Xiadian deposit	−450	Stage II	Gold-bearing Qz + Py veinlets in altered wallrock	17XD26			17XD26		
	−450	Stage II	Gold-bearing Qz + Py vein	17XD16	17XD16	17XD16	17XD16		
	−450	Stage II	Gold-bearing Qz + Py vein	17XD15	17XD15		17XD15		
	−525	Stage II	Gold-bearing Qz + Py vein	17XD12	17XD12		17XD12	17XD12	
	−652	Stage II	Gold-bearing Qz + Py vein	17XD11	17XD11		17XD11		
	−652	Stage II	Gold-bearing Qz + Py veinlets in altered wallrock	17XD02	17XD02	17XD02	17XD02		17XD02
Jiangjiayao deposit	−1512	Stage II	Gold-bearing Qz + Py veinlets in altered granite	17JJY07	17JJY07				
	−1513	Stage II	Gold-bearing Qz + Py veinlets in altered granite	17JJY14	17JJY14				
	−1529	Stage II	Gold-bearing Qz + Py veinlets in altered granite	17JJY15			17JJY15	17JJY15	
	−1565	Stage II	Gold-bearing Qz + Py veinlets in altered granite	17JJY24-1, 17JJY24-2	17JJY24-2	17JJY24-1, 17JJY24-2	17JJY24-1, 17JJY24-2	17JJY24-1, 17JJY24-2	

Notes: The elemental and isotopic data are listed in Table S1 and S2. Abbreviations: Qz = quartz; Py = pyrite.

−5.7‰ for HYC-1, obtained by stable isotope mass spectrometry) within errors.

5. Results

5.1. Occurrence and microtextures of pyrite and gold

In the Linglong-type mineralization (Linglong deposit), pyrite of hydrothermal stage I (Py1) mainly occurs as disseminated grains in altered granite while those of the stage II (Py2) and III (Py3) occur in quartz + polymetallic sulfide veins (Fig. 4a–e). The Py1 grains are Au-barren, euhedral to subhedral (mainly cubic crystals) and 0.2–1 mm in size (Fig. 5a). They are commonly homogenous in texture, but contain some silicate inclusions. The Py2 and Py3 grains are Au-bearing, hosting µm-scale visible gold grains as inclusions or in fractures (Fig. 5b–c). These pyrite grains are subhedral to anhedral, varying widely in size from several millimeters to centimeters. Under the BSE imaging, the Py2 and Py3 grains do not show significant zoning, but the Py2 grains are bright and "clean" while the Py3 grains are dark and "dirty" (Fig. 6a–b). The Py3 grains typically host polymetallic sulfide (e.g., chalcopyrite, pyrrhotite, galena and sphalerite) inclusions (Fig. 5c and 6b). Locally, a Py2 grain contains grey (Py2a) and dark (Py2b) zones, of which the dark zones cut the grey zones (Fig. 6c). The grey zones are relatively "clean" and homogeneous while the dark zones host numerous sulfide inclusions. The Py2b is difficult to distinguish from the Py3 under the BSE imaging, but it has distinct elemental and isotopic compositions, as revealed by the LA-(MC)-ICP-MS analyses.

In the Jiaojia-type mineralization (Jiangjiayao and Xiadian deposits), the Au-bearing Py2 grains are disseminated in the altered granite or occur in the quartz + sulfide veinlets (Fig. 4f-i). They also host µm-scale visible gold grains as inclusions or in fractures (Fig. 5d-e), but contain Bi-Te-S minerals (mainly tetradymite, Bi_2Te_2S) not seen in the Linglong samples (Fig. 5f). Compared with those of the Linglong-type mineralization, these pyrite grains are more anhedral and porous with abundant silicate (e.g., sericite) inclusions (Fig. 6d).

The gold grains in the three deposits are granular or irregular with sizes varying from several microns to hundreds of microns (Fig. 5b-e). They are commonly larger in the Linglong-type than in the Jiaojia-type mineralization. FIB-TEM analyses indicate that the gold grains are inhomogenous in texture and composition, which have sector or oscillatory zoning (Fig. 6e–f). At an enlarged scale (e.g., 1–10 nm), it shows that a coarse gold grain in the Linglong-type mineralization is composed of several irregular
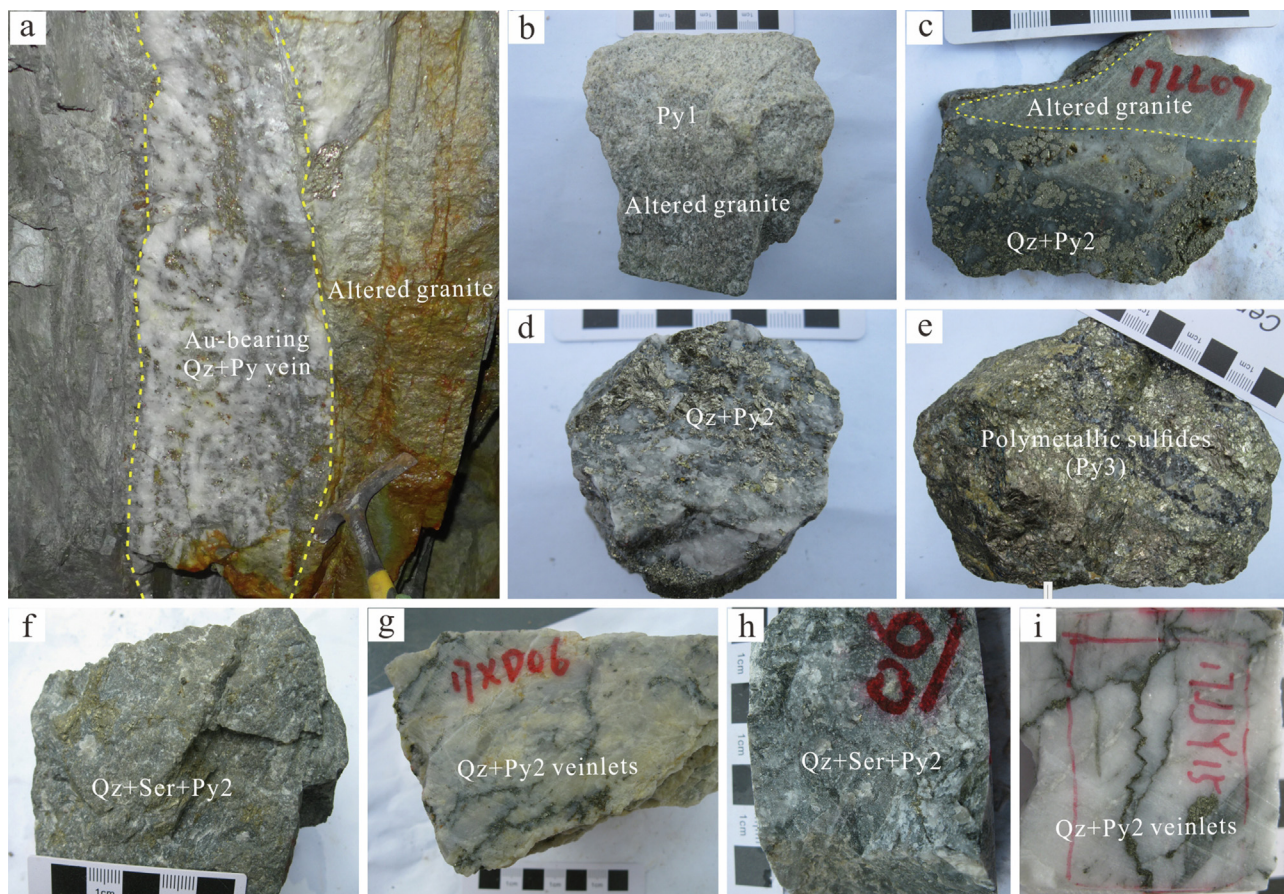
Fig. 4. Hydrothermal stages and ores from the Linglong (a–e), Xiadian (f, g) and Jiangjiayao (h, i) gold deposits. (a) The Ling-type mineralization showing Au-bearing Qz + Py vein in the altered granite. (b) Py1 grains of hydrothermal stage I disseminated in the altered granite. (c) Qz + Py vein of hydrothermal stage II cuts the altered granite. (d) and (e) Typical ores of hydrothermal stage II and III from the Linglong-type mineralization, respectively. (f) and (g) Disseminated and stockwork mineralization of hydrothermal stage II from the Xiadian gold deposit, respectively. (h) and (i) Disseminated and stockwork mineralization of hydrothermal stage II from the Jiangjiayao gold deposit, respectively. Abbreviations: Qz, quartz; Py, pyrite; Ser, sericite.
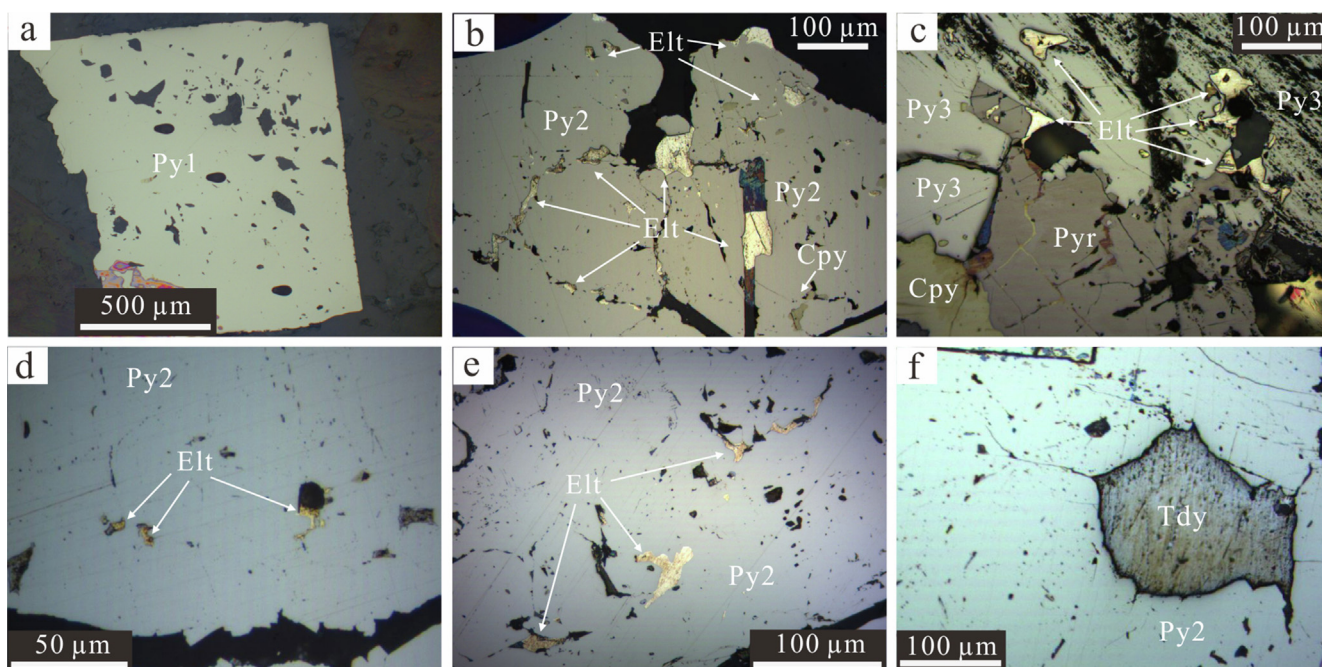

Fig. 5. Occurrence of pyrite and gold and their relationships. (a) Euhedral and coarse Py1 grain from the Linglong gold deposit. (b) and (c) Gold grains of hydrothermal stage II and III from the Linglong gold deposit, both occurring as inclusions or in the fractures of pyrite. (d) and (e) Gold grains of hydrothermal stage II from the Jiangjiayao and Xiadian gold deposits, respectively. (f) Tetradymite occurring within Py2 from the Xiadian deposit. Abbreviations: Py, pyrite; Pyr, pyrrhotite; Cpy, chalcopyrite; Elt, electrum.
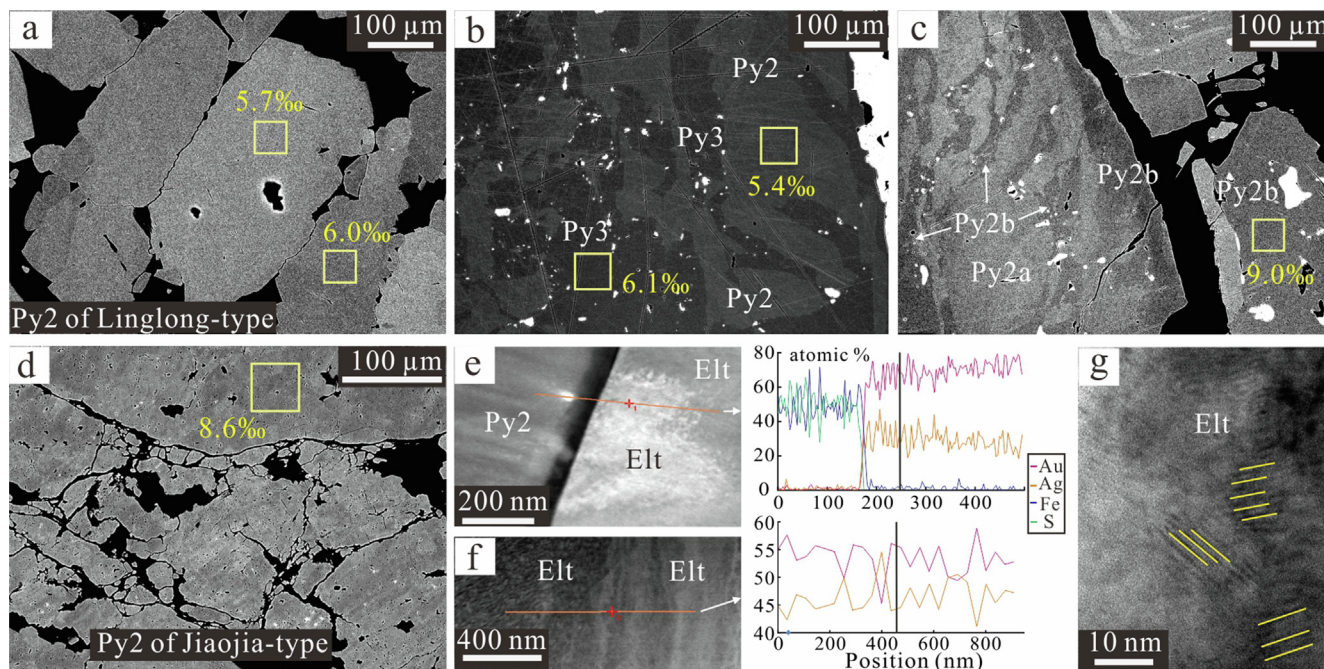
Fig. 6. BSE and FIB-TEM imaging of pyrite and gold. (a) BSE image of Py2 from the Linglong gold deposit, showing homogenous texture. (b) BSE image of Py2 and Py3 from the Linglong gold deposit, showing that the Py2 is cut by the Py3 and the Py3 contains many sulfide inclusions. (c) BSE image of Py2a and Py2b from the Linglong gold deposit, showing that the Py2b contains many sulfide inclusions and cuts the Py2a. (d) BSE image of Py2 from the Xiadian gold deposit, showing porous texture with abundant tiny mineral inclusions. (e) FIB-TEM imaging of pyrite and gold (17LL07) from the Linglong gold deposit, showing the distinct contact between the pyrite and gold and the inhomogeneous texture and composition of gold. (f) Gold grain from the Linglong gold deposit is inhomogeneous in texture under the FIB-TEM imaging. (g) A coarse gold grain from the Linglong gold deposit is composed of irregular nanoparticles with variable lattice plane orientations under the FIB-TEM imaging. The representative spots analyzed for $\delta^{34}S$ are also shown with yellow color in a-d.

nanoparticles with variable lattice plane orientations (Fig. 6g), similar to those identified in high-grade gold veins formed through flocculation of colloidal gold nanoparticles (McLeish et al., 2021).

5.2. Gold fineness of electrum

Gold grains are mainly electrum. Gold fineness of electrum varies widely from 398 to 863 (Table S1). Temporally, from the Py2 to the Py3 stage in the Linglong deposit, the fineness decreases from 603–819 (mean of 690) to 398–614 (mean of 511). Spatially, from the deep (altitude of −1600 to −1512 m) to the shallow (altitude of −652 to −450 m) depths in the Jiangjiayao and Xiadian
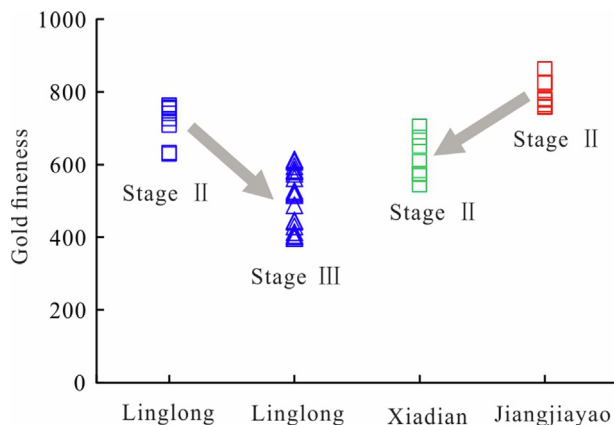

Fig. 7. Variations of gold fineness from the Linglong, Xiadian and Jiangjiaoyao gold deposits.

deposits, the fineness decreases from 758–863 (mean of 794) to 544–706 (mean of 613) (Fig. 7).

5.3. Elemental compositions and distributions in pyrite

About 569 spots for elemental concentration and 9 mappings for elemental distribution were conducted on pyrite from the three deposits. Vanadium, Cr, Mn, Co, Ni, Cu, Zn, Ge, As, Se, Ag, Sb, Au, Bi and Pb are commonly detectable, but vary widely in concentration (Table S2). Arsenic is the most abundant element among the above trace elements, showing tens to hundreds of ppm. Cobalt, Ni, Cu, Zn, Se, Pb and Bi are less abundant, varying from several to tens of ppm. Other elements such as V, Cr, Mn, Ge, Ag and Sb range from<1 ppm to several ppm. Gold concentrations are commonly<1 ppm (tens to hundreds of ppb) and do not differ between different hydrothermal stages or mineralization styles, but generally show a positive correlation with Ag and As (Fig. 8a–b). The Bi concentrations decrease continuously from the Jiaojiayao to the Xiadian and then to the Linglong samples, seeming to be depth-dependent. Gold is not well correlated with Bi (Fig. 8c), but Ag is positively correlated with Bi and the Au/Ag ratio generally decreases with increasing Bi (Fig. 8d–e). From the early to the late hydrothermal stages, Cu, Zn, Pb and Ag concentrations increase from the Py1 to the Py2a and then to the Py3, but vary widely in the Py2b of the Linglong deposit (Fig. 8f–h). Silicon and Al cannot enter into the lattice of pyrite, but they were detected due to the presence of silicate mineral inclusions, showing much higher concentrations in the Jiaojia-type than in the Linglong-type mineralization (Fig. 8i).

LA-ICP-MS elemental mapping shows that Au correlates well with As and Te, while Ag correlates with Cu, Zn, In, Sn, Sb, Pb and Bi (Fig. 9).
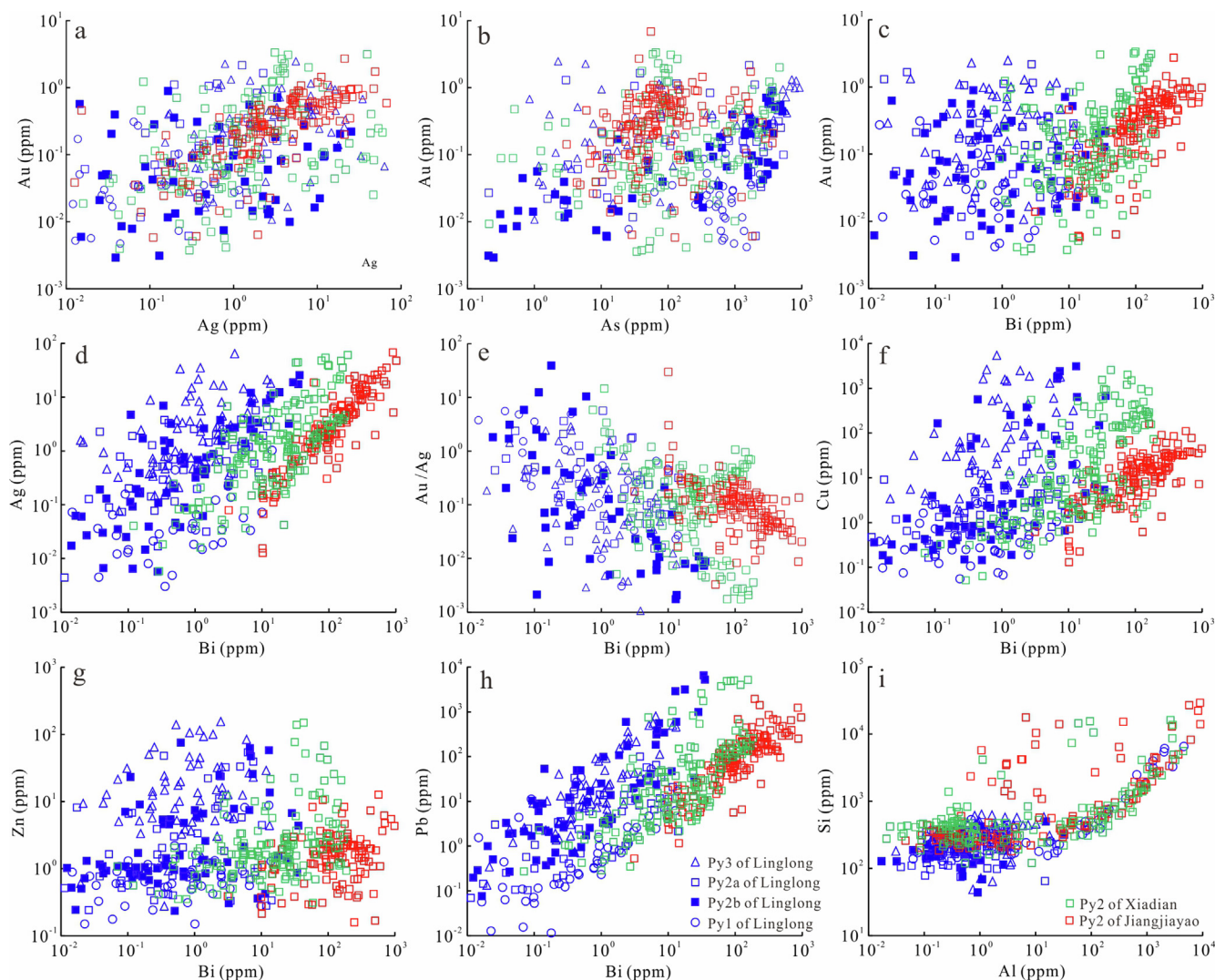
Fig. 8. Covariant diagrams of Au vs. Ag (a), Au vs. As (b), Au vs. Bi (c), Ag vs. Bi (d), Au/Ag vs. Bi (e), Cu vs. Bi (f), Zn vs. Bi (g), Pb vs. Bi (h), Si vs. Al (i) for the pyrite from the Linglong, Xiadian and Jiangjiayao deposits.

5.4. Sulfur isotopic compositions of pyrite

About 294 spots for sulfur isotopic composition were conducted. The $\delta^{34}S$ of pyrite in the studied samples varies between 4.8‰ and 12.8‰ (Table S2). From the Py1 to the Py2a and then to the Py3 in the Linglong deposit, the $\delta^{34}S$ keeps stable and low (4.8–7.6‰, mean of 6.1‰). It shows a remarkable increase in the Py2b (6.0–12.8‰, mean of 9.5‰), which is positively correlated with As and Au concentrations (Fig. 10a–b). The $\delta^{34}S$ values of Py2 in the Jiangjiayao and Xiadian deposits (5.2–9.8‰, mean of 7.4‰) are similar to each other, which are coupled with elevated Al and Si concentrations (Fig. 10c).

6. Discussion

6.1. Gold endowment of mantle and crustal endmembers

Neither magmatic nor metamorphic events have been found to be genetically associated with the giant gold mineralization in the Jiaodong Peninsula, leading to the arguments which source supplied the huge amounts of gold. Various geological units, such as the Precambrian basement rocks (Wang et al., 1989; Xu, 1998),

the Mesozoic granitoids (Chen et al., 2005; Yan et al., 2014), the metasomatized lithospheric mantle (Deng et al., 2020b; Wang et al., 2020), and the subducted oceanic slab (Goldfarb and Santosh, 2014; Groves and Santosh, 2016; Zhu and Sun, 2021), have been proposed as the source. Previous studies found that the $\delta^{34}S_{pyrite}$ values of ores vary widely from 2‰ to 14‰ (Deng et al., 2020b), which almost cover all the $\delta^{34}S$ ranges of wallrocks in the study region (Fig. 11). The previously obtained $\delta^{34}S$ values were mainly measured by whole-rock analytical methods, which might be the mixed compositions of different generations of pyrite. Based on the in-situ analyses, three groups of $\delta^{34}S_{pyrite}$ are distinguished in the studied deposits. Group 1 shows relatively low and stable $\delta^{34}S$ from the early to the late hydrothermal stages in the Linglong-type mineralization (Fig. 10a–b). Because the ore lodes in this type of mineralization cut the wallrocks with distinct boundaries and are composed of simple mineral assemblages of quartz + sulfides (Fig. 4a-e), the slight $\delta^{34}S$ variations indicate that significant external contamination or sulfur isotopic fractionation might have not occurred during the fluid evolution. The $\delta^{34}S$ values thus can represent the original sulfur isotopic compositions of the fluid, suggesting a low-$\delta^{34}S$ (low to ~ 5‰) endmember auriferous fluid for the gold mineralization. The low $\delta^{34}S$ values fall into the ranges of the late Archean metamorphic rocks (mean of ~ 5.4‰)
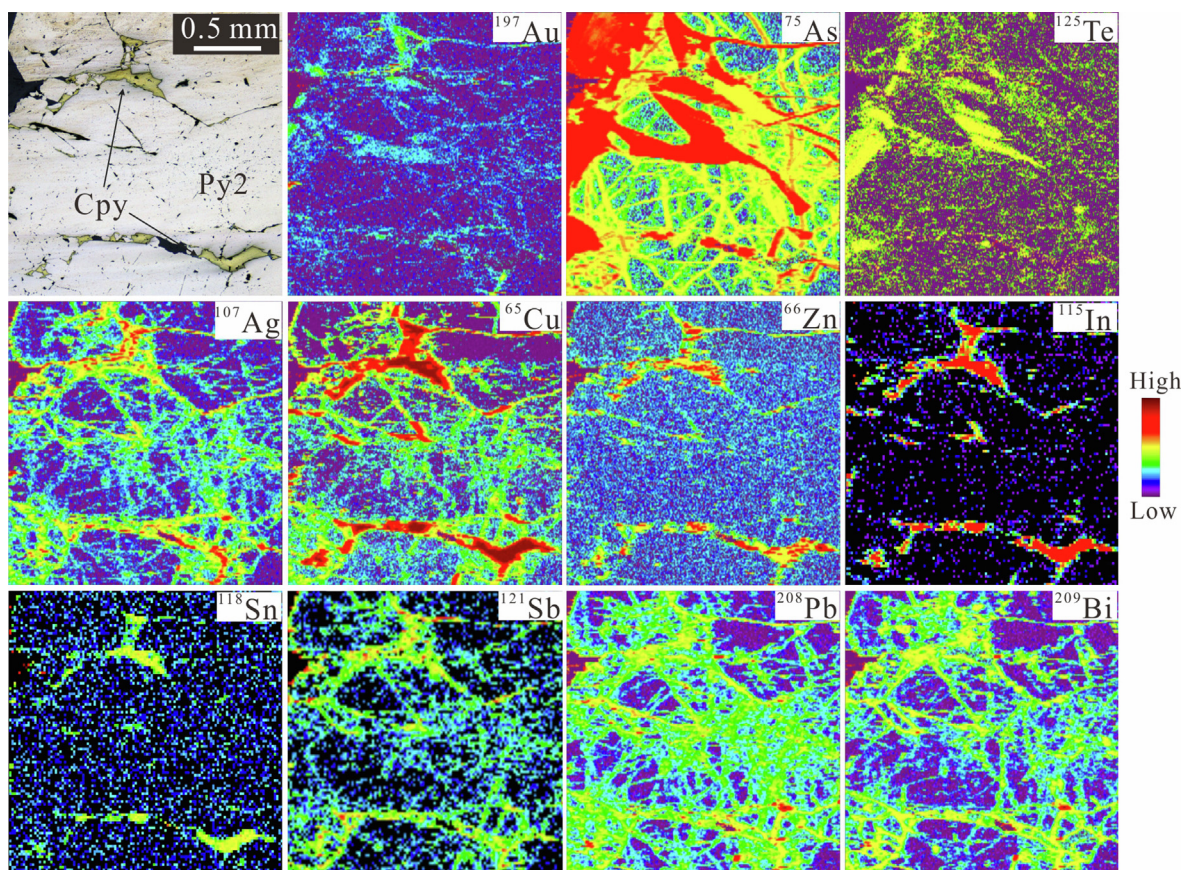
Fig. 9. LA-ICP-MS elemental mapping of Py2 (17LL09) from the Linglong gold deposit.
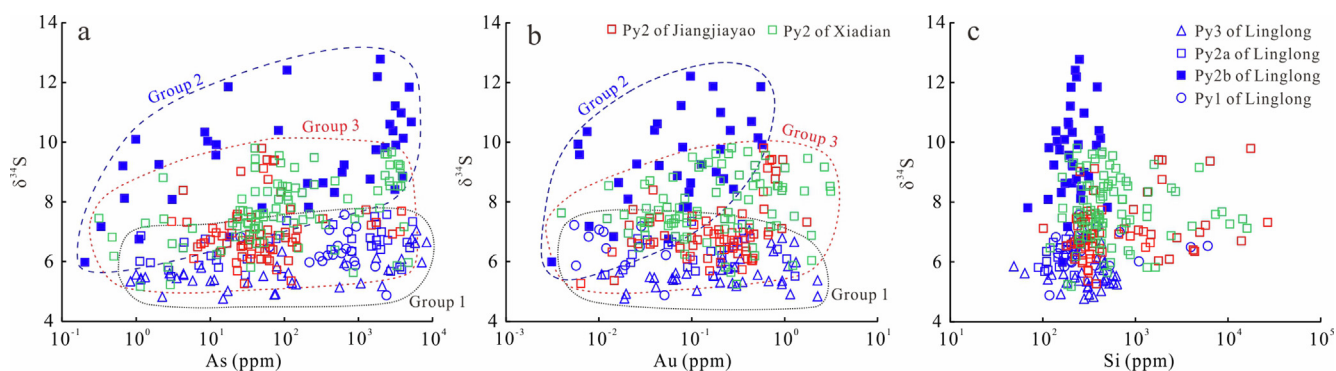

Fig. 10. Covariant diagrams of $\delta^{34}S$ vs. As (a), $\delta^{34}S$ vs. Au (b) and $\delta^{34}S$ vs. Si (c) for the pyrite from the Linglong, Xiadian and Jiangjiayao gold deposits.

and the early Cretaceous mafic dykes (mean of $\sim 5.8‰$) (Fig. 11). The late Archean metamorphic rocks were metamorphosed at ~ 2.5 Ga (Jahn et al., 2008), which could not be responsible for the generation of the auriferous fluids. The mafic dykes are widespread in the goldfields and formed almost contemporaneously with the gold mineralization (Li et al., 2016; Deng et al., 2017), implying their the same or similar source. The mafic dykes were mainly derived from the subcontinental lithospheric mantle (Li et al., 2016; Deng et al., 2017). Combined with other isotopic compositions (e.g., C-O-Sr-Nd-Pb-He-Ar) also showing significant involvement of mantle components in the gold deposits (Mao et al., 2008; Li and Santosh, 2014; Tan et al., 2018; Deng et al., 2020a, 2020b), it is inferred that the low-$\delta^{34}S$ auriferous fluids were derived from a mantle or mantle-related source. Actually, the low-$\delta^{34}S$ values (<7‰) of pyrite have been widely identified

in the Jiaodong gold deposits, such as the Taishang, Jintingling and Dayingezhuang gold deposits in the Zhaoyuan-Laizhou belt (Yang et al., 2016b; Ma et al., 2018; Yuan et al., 2019), and the Daliuhang and Hushan gold deposits in the Penglai-Qixia belt (Yang et al., 2018; Feng et al., 2020). This indicates that the low-$\delta^{34}S$ auriferous fluids were universal in the Jiaodong Peninsula and thus might be the primary auriferous fluids for the giant gold mineralization.

Group 2 shows a clear increase of $\delta^{34}S$ accompanied by increasing As and Au concentrations in the Py2b from the Linglong deposit (Fig. 10a-b). The variations of $\delta^{34}S$ can be induced by sulfur isotopic fractionations (equilibrium and Rayleigh) between the sulfur-bearing minerals and the fluids, which are commonly controlled by temperature, pressure, oxygen fugacity, pH and Rayleigh process (Ohmoto, 1972; Hutchison et al., 2020). Thermodynamic mod-
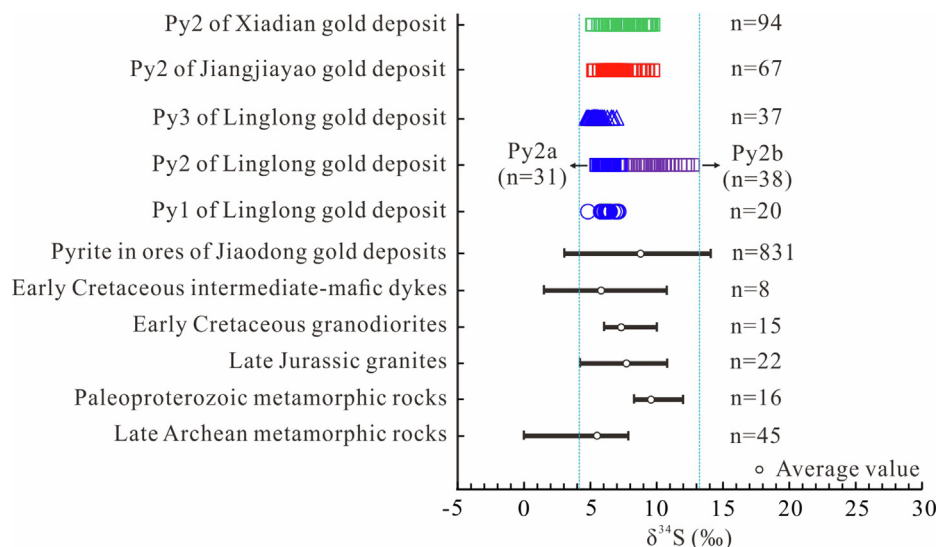
Fig. 11. Summary of $\delta^{34}S$ from the studied gold deposits, Jiaodong gold deposits and different geological units in the Jiaodong Peninsula. The data of Jiaodong gold deposits and different geological units are from the summarized dataset by Deng et al. (2020b).

elling on sulfur isotopic equilibrium fractionation at the physico-chemical conditions of the studied deposits shows that as the temperature decreases to 300–250 °C with the oxygen fugacity of pyrite-pyrrhotite buffer (Fig. 5c) and the pH of 3–4 (Wang et al., 2022), no significant fractionation will occur between the pyrite and the fluids (Fig. 12a–b). This indicates that the increase of $\delta^{34}S$ cannot be explained by sulfur isotopic equilibrium fractionation. Rayleigh fractionation under the above conditions will lead to the decrease of $\delta^{34}S_{pyrite}$ at the temperature range of 350–250 °C (Fig. 12c–d), also inconsistent with the increase of $\delta^{34}S_{pyrite}$. Rock-buffered reduction can lead to the continuous increase of $\delta^{34}S_{pyrite}$ (Ward et al., 2017), but as mentioned before, fluid-rock interaction is insignificant in the Linglong deposit and there is no evidence for reduction due to the constant mineral assemblages of quartz + sulfides throughout the hydrothermal evolution. Rapid decompression (e.g., fluid boiling or flash vaporization) with injection of rock-buffered fluids can cause large variations of $\delta^{34}S_{pyrite}$ (extremely negative to positive) to micron scale (Peterson and Mavrogenes, 2014). This process (or likewise) seems to occur in the studied deposit, considering that fluid boiling has been widely identified in the ore-forming stages of the Linglong deposit (Wen et al., 2015; Guo et al., 2020; Wang et al., 2022). Combined with the Py2b cutting the Py2a as networks at the micron scale (Fig. 6c), it is inferred that another pulse of fluid characterized by elevated $\delta^{34}S$ (Py2b) was injected into the primary fluids (Py2a), which might be driven by fault-valve process (Peterson and Mavrogenes, 2014). The $\delta^{34}S$ of Group 2 is high up to $\sim 13‰$, and even up to > 20‰ in the neighboring gold deposits (Hu et al., 2020b, 2022). These high $\delta^{34}S$ values are quite different from those of the late Archean metamorphic rocks and the Mesozoic granitoids and mafic dykes, but closer to the Paleoproterozoic metamorphic rocks in the study region (Fig. 11). The protoliths of the Paleoproterozoic metamorphic rocks are mainly neritic sediments deposited in an active continental margin (Xu and Liu, 2019), which could provide the high-$\delta^{34}S$ materials due to the presence of seawater sulfate (Chang et al., 2008; Farquhar et al., 2010). In addition, the marine sediments can be enriched in As and Au (Large et al., 2011), consistent with the coupled increase of As and Au (Fig. 10a–b). It is thus inferred that the high-$\delta^{34}S$ auriferous fluids were resulted from the primary low-$\delta^{34}S$ auriferous fluids leaching additional S, As and Au from the Precambrian metasedimentary host rocks. Hydrothermal fluid leaching S, As and Au from wallrocks is not rare to see, especially in the

Carlin-type gold deposits (Cline et al., 2005; Kesler et al., 2005; Emsbo et al., 2006; Large et al., 2011). Considering that the present-day Paleoproterozoic metamorphic rocks in the study region are low in S (38–303 ppm) and Au (0.66–1.92 ppb) contents (Wang et al., 2021), S-As-Au-rich sequences might be formed during the Precambrian metamorphism and stored somewhere within the metamorphic rocks. This can be supported by the high-$\delta^{34}S$ (>10‰) pyrite frequently identified in the neighboring gold deposits from the northwestern Jiaodong Peninsula (e.g., Sanshandao, Xinli, Xincheng, Jiaojia and Wangershan deposits, Mills et al., 2015; Hu et al., 2020b, 2022; Peng et al., 2021), where Paleoproterozoic metasedimentary rocks are widespread (Fig. 1). Recent Sr-Pb isotopic studies on scheelite and galena from the Xiadian and Majiayao gold deposits corroborate the contribution of ore-forming metals from the Proterozoic rocks (Liu et al., 2021). Actually, the latest studies on gold mobilization in the Proterozoic clastic sedimentary rocks from the Jiao-Liao-Ji Belt show that high amounts of Au can be efficiently mobilized (release of $\sim 52\%$) during the prograde metamorphism and preserved somewhere in the metamorphic rocks, which likely contributed significantly to the giant gold mineralization in the eastern NCC (Cui et al., 2022).

Group 3 shows moderate $\delta^{34}S$ coupled with elevated lithophile elements such as Al and Si in the Jiaojia-type mineralization (Fig. 8i and 10c). Because Al and Si can hardly enter into the lattice of pyrite, the high Al and Si contents could not be resulted from co-precipitation from the auriferous fluids, but might be incorporated into the pyrite as mineral inclusions. This is corroborated by the petrographic evidence showing that the pyrite in the Jiangjiayao and Xiadian deposits commonly contains many tiny silicate (e.g., sericite) inclusions with porous texture (Fig. 6d). Actually, the direct wallrocks of the orebodies in the above two deposits are the late Jurassic granites which have high Al and Si contents and show consistent $\delta^{34}S$ values with those of the Group 3 (Fig. 11). They are thus capable of providing abundant Al and Si and appropriate S isotopes to the pyrite. Combined with all the above features, it is deduced that the increase of $\delta^{34}S$ as well as Al and Si contents in the Py2 of the Jiaojia-type mineralization were resulted from the enhanced fluid-rock interaction between the auriferous fluids and the granitic wallrocks. It is noteworthy that, compared with the Group 2 in the Linglong-type mineralization, more lithophile elements rather than ore-forming metals were leached from the wallrocks due to the depletion of As and Au in the granites.
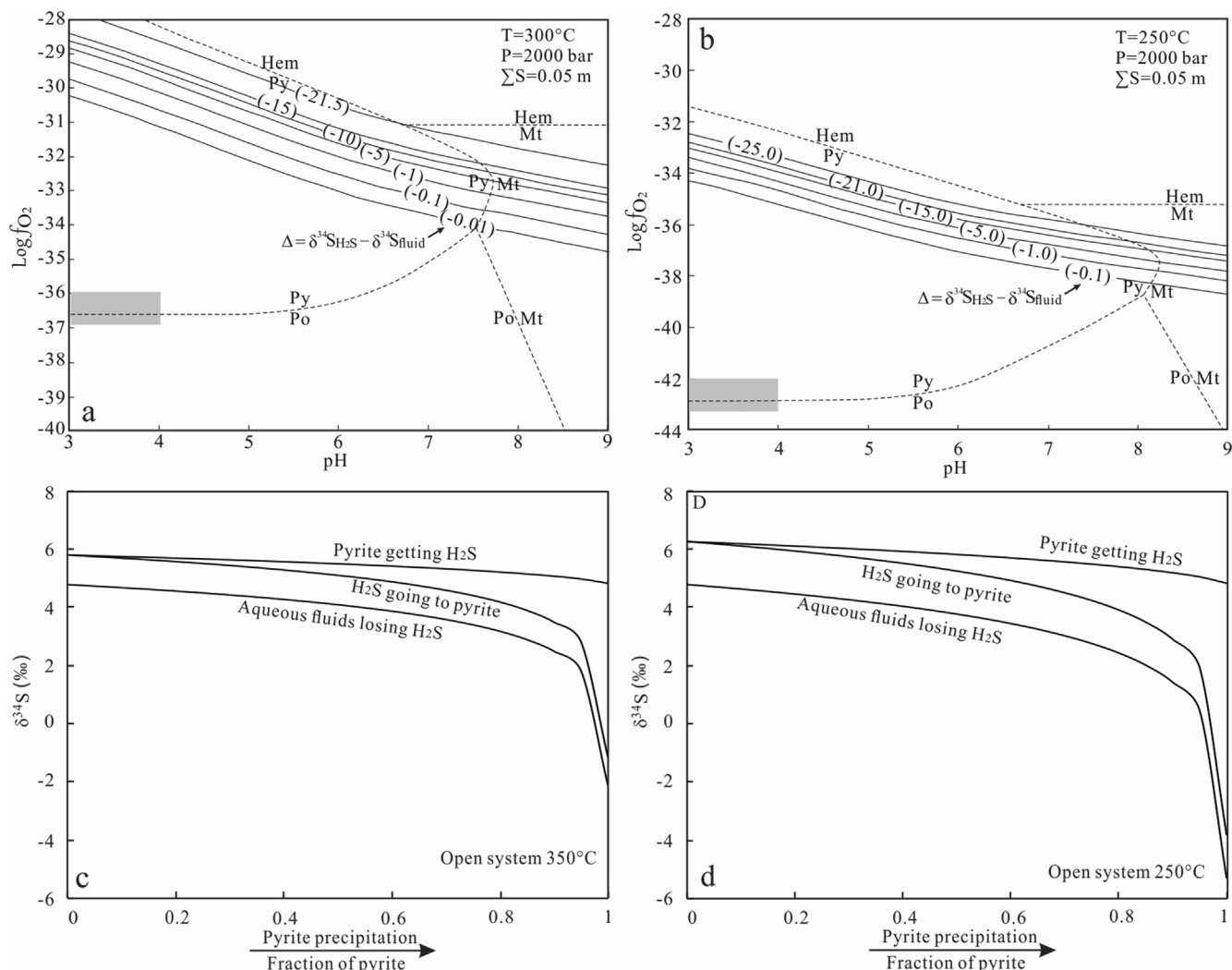
Fig. 12. Thermodynamic modelling on sulfur isotopic fractionation at different physicochemical conditions. (a) and (b) Sulfur isotopic equilibrium fractionation between H_2S and total S of ore-forming fluids as the function of pH and oxygen fugacity (f_{O_2}) with fixed temperature (300 °C and 250 °C, respectively), pressure and $\sum S$. The grey zone represents the f_{O_2} and pH conditions of the studied fluids. (c) and (d) Rayleigh fractionation of $\delta^{34}S$ at different temperatures (350 °C and 250 °C, respectively). The modelling methods and parameters follow Ohmoto (1972), Evans et al. (2014) and Crossley et al. (2018).

6.2. Gold deposition in different structural settings

The Linglong- and Jiaojia-type mineralization styles have been considered to occur in different structural settings, of which the former mainly occurs in the tensional fractures while the latter occurs in the transpressional faults (Song et al., 2015; Deng et al., 2019; Fan et al., 2021). It is found that both mineralization styles almost have the same ore-forming fluids (Wen et al., 2015; Guo et al., 2017), but show differences in mineral texture, elemental and isotopic compositions (Figs. 6, 8 and 10). These phenomena imply that the Au in the two mineralization styles was probably transported by the same way, but deposited through different processes.

In the Linglong deposit, the Au was dominantly deposited in stage II with some in stage III (Figs. 4 and 5). From stage II to III, the base metals (e.g., Cu, Zn and Pb) show increasing deposition while the gold fineness decreases continuously (Figs. 7 and 8). Gold deposition can be induced by the changes of temperature, pressure, acidity, salinity, oxygen and sulfur fugacities, which are commonly associated with the geological processes such as fluid cooling, mixing/unmixing and fluid-rock interaction (Mikucki, 1998; Williams-Jones et al., 2009; Pokrovski et al., 2014). The

homogenization temperatures of fluid inclusions in the Linglong deposit and in most of the Jiaodong gold deposits decrease from the pre-mineralization stage (stage I, 350 ± 70 °C) to the ore-forming stages (stage II and III, 250 ± 100 °C) with salinities changing slightly (Fan et al., 2007; Li et al., 2015; Wen et al., 2015; Wang et al., 2022). This indicates that cooling occurred. However, detailed comparisons show that the homogenization temperatures between the stage II and III change little (Wen et al., 2015; Guo et al., 2020; Wang et al., 2022), which cannot fully explain the variations of base metals and gold fineness. The $\delta^{34}S$ of Group 1 keeps stable throughout the hydrothermal evolution (Fig. 10a-b), in combination with the simple mineral assemblages of quartz + sulfides, indicating that significant wallrock contamination and drastic changes in oxygen fugacity did not occur. Coexistence of different types of fluid inclusions (e.g., liquid-rich, vapor-rich and CO_2-rich) with similar homogenization temperatures widely occurs in the Linglong deposit (Wen et al., 2015; Guo et al., 2020; Wang et al., 2022), strongly suggesting fluid unmixing/boiling (Ramboz et al., 1982). Fluid unmixing can lead to the release of CO_2 into the vapor phase, increasing the pH of the liquid phase (Drummond and Ohmoto, 1985; Kokh et al., 2017). According to the PTX-pH properties of H_2O-CO_2-NaCl system, in combination with the CO_2

contents of fluid inclusions decreasing from the early to the late hydrothermal stages in the Linglong deposit (Wang et al., 2022), more than 1 unit of pH could be elevated (pH from ~ 3 to > 4) due to the CO_2 degassing (Fig. 13a). Experimental and thermodynamic studies show that the solubilities of Au as well as Cu, Zn and Pb decrease sharply from acidic (e.g., pH < 3) to neutral conditions (e.g., pH of 4–6) in the reduced, moderate- to low-temperature (e.g., 200–400 °C) and low-salinity (e.g., 1–2 m NaCl) H-O-S-Cl fluids (Reed and Palandri, 2006; Pokrovski et al., 2013, 2014). An increase of pH within the above range would lead to the efficient metal deposition (Fig. 13b–c). This is consistent with the increasing deposition of base metals from the stage II to III. More importantly, gold fineness is highly dependent on pH in a moderate- to low-temperature, low-salinity, S-bearing hydrothermal fluid (Gammons and Williams-Jones, 1995; Pal'yanova, 2008; Liang and Hoshino, 2015), which will decrease as the pH increases (Fig. 13d–e). The decrease of gold fineness from the stage II to III matches with the increase of pH. It is thus inferred that the pH increasing from the early to the late hydrothermal stages, induced by CO_2 degassing during fluid boiling, led to the remarkable Au deposition. Actually, fluid boiling can also explain the formation of visible gold. As mentioned before, gold mainly occurs as μm-scale visible grains in the pyrite (Fig. 5b-e). Visible gold can be generated through remobilization of previous lattice-bound Au into the fractures of the recrystallized or newly formed pyrite (Morey et al., 2008; Cook et al., 2013; Fougerouse et al., 2016), or through aggregation of Au nanoparticles (Saunders and Burke, 2017; Hastie

et al., 2021; McLeish et al., 2021). In the Linglong deposit, the Au could not be remobilized due to the low Au concentrations in the pyrite (Fig. 8a). In addition, the pyrite grains hosting visible gold commonly show single-stage growth (Figs. 5 and 6), indicating the direct precipitation without recrystallization. It is noted that the gold grains have inhomogeneous textures and compositions on the nanoscale (Fig. 6e–f). This indicates that drastic changes of physicochemical conditions occurred. The FIB-TEM analyses show that a coarse gold grain can consist of numerous nanoparticles (10–20 nm) with variable lattice plane orientations (Fig. 6g), suggesting the aggregation of Au nanoparticles (McLeish et al., 2021). It has been proposed that fluid boiling can not only cause the formation of gold nanoparticles (Gartman et al., 2018; McLeish et al., 2021), but also promote particle sticking by increasing the particle velocities to overcome surface-charge repulsions (Saunders and Burke, 2017), leading to the generation of coarse gold grains.

In the Jiangjiayao and Xiadian deposits, the pyrite grains are much more porous and "dirty" than those of the Linglong deposit (Fig. 6). In addition, the pyrite grains contain abundant silicate inclusions with elevated lithophile elemental contents (Fig. 6d and 8i). These phenomena indicate that enhanced fluid-rock interaction occurred in the Jiaojia-type mineralization. Under this condition, the Au deposition was likely induced by the loss of H_2S during fluid-rock interaction (Pokrovski et al., 2014; Hu et al., 2020a). In moderate- to low-temperature (<400 °C), low-salinity, weakly acidic and reduced S-bearing fluids, Au is mainly
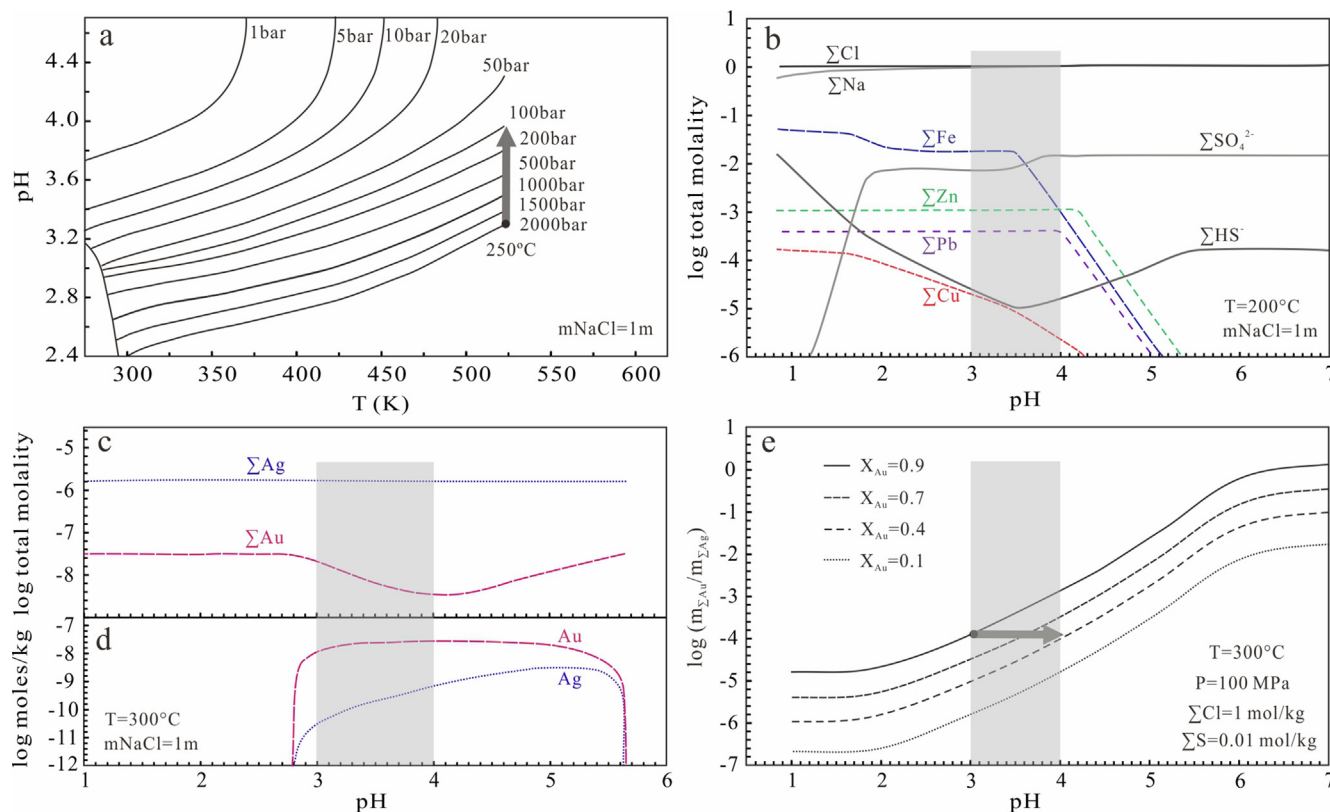

Fig. 13. Thermodynamic modelling and experimental results of pH and the effects of pH on metal solubilities (Au, Ag, Fe, Cu, Zn and Pb) and gold fineness in hydrothermal fluids. (a) Calculated pH values of H_2O-CO_2-NaCl system at various temperatures and pressures (after Li and Duan, 2007), showing that the pH will increase as the pressure decreases at a given temperature. (b) Solubilities of Fe, Cu, Zn and Pb decease as the pH increases from the acidic to the neutral conditions in the S-bearing H_2O-NaCl fluid (after Reed and Palandri, 2006). (c) and (d) Solubility of Au decreases as the pH increases from the acidic to the neutral conditions in the S-bearing H_2O-NaCl fluid, leading to the deposition of electrum with decreasing gold fineness (after Reed and Palandri, 2006). (e) Gold fineness (X_{Au}) of electrum equilibrated with H_2O-Cl-S fluid decreases as the pH increases (after Liang and Hoshino 2015). The temperatures of 250–300 °C, pressures of 100–200 MPa and salinity of 1 m NaCl generally represent those of the studied fluids (Wen et al., 2015; Chai et al., 2017; Liu et al., 2018; Guo et al., 2020; Wang et al., 2022). The pH values calculated for the studied fluids are mainly 3–4, marked by grey color in the diagrams.

transported as hydrogen sulfide species (e.g., $Au(HS)_2^-$ and $AuHS^0$, Mikucki, 1998; Williams-Jones et al., 2009; Pokrovski et al., 2014; Trigub et al., 2017). Pyrite can be favorably generated during the fluid-rock interaction due to the granitic wallrocks supplying Fe (from Fe-bearing minerals, such as biotite being altered to sericite, Fig. 4f), leading to the consumption of H_2S and thus the breakdown of Au hydrogen sulfide species (Hu et al., 2020a, 2022). Thermodynamic modelling shows that under the studied fluid conditions, the decrease of H_2S can reduce the Au solubility up to 1–2 orders of magnitude at the temperature range of 350–250 °C (Fig. 14), being efficient for Au deposition.

6.3. Gold deposition through depth

Gold deposition lasted along the depth profile of 0–4 km in the Jiaodong gold deposits (Wen et al., 2016), within which the homogenization temperatures and salinities of fluid inclusions change slightly in the same hydrothermal stage (Wen et al., 2016; Liu et al., 2018). This implies that the auriferous fluids might keep stable during upward transportation. However, the compositions of electrum show that the gold fineness is much higher and homogeneous in the deepest samples (758–863 at the depths of −1510 to −1600 m), but decreases significantly in the shallower samples (544–706 at the depths of −450 to −652 m) and varies widely in the shallowest samples (398–819 at the depths of −10 to −50 m) (Fig. 7 and Table S1). The vertical change of gold fineness has been identified in the other Jiaodong gold deposits (Peng et al., 2021), establishing this a common phenomenon in the study

region. The decrease of gold fineness is accompanied by the decreasing Bi concentrations in pyrite (Figs. 7 and 8). These trends indicate that there might be a depth- or temperature-dependent factor controlling the vertical Au deposition. Thermodynamic and experimental studies show that the solubility of Bi in hydrothermal fluids is highly dependent on temperature, which will decrease by 1–2 orders of magnitude as the temperature decreases below 400 °C (Tooth et al., 2013). Cooling of the hydrothermal fluid during upward transportation would significantly reduce the Bi solubility. The Bi-Te-S minerals occur in the deep samples of the Jiangjiayao and Xiadian deposits (Fig. 5f), corroborating that the Bi was preferentially scavenged from the fluids at the high-temperature conditions (Cook et al., 2007). Gold and Ag can be strongly fractionated into Bi-Te-S complexes (Cook and Ciobanu, 2004; Ciobanu et al., 2010; Voronin and Osadchii, 2013), of which the Ag seems to be more fractionated than Au in the studied deposits, as indicated by the Bi-Te-S minerals containing abundant Ag (150–3000 ppm) but little Au (Table S1). The well correlated Ag and Bi in the deep pyrite samples also support the high affinity of Ag to Bi under the high-temperature conditions (Fig. 8d). More importantly, the Au/Ag ratio in pyrite shows a negative correlation with Bi (Fig. 8e), corroborating that the Bi contributed to fractionate Au and Ag. Therefore, it is deduced that due to the Ag being more fractionated into the Bi-Te-S minerals at high temperatures, the gold fineness decreased as the Ag gradually entered into the electrum during upward transportation.

This temperature-dependent variation seems to contradict with the homogenization temperatures of fluid inclusions which do not
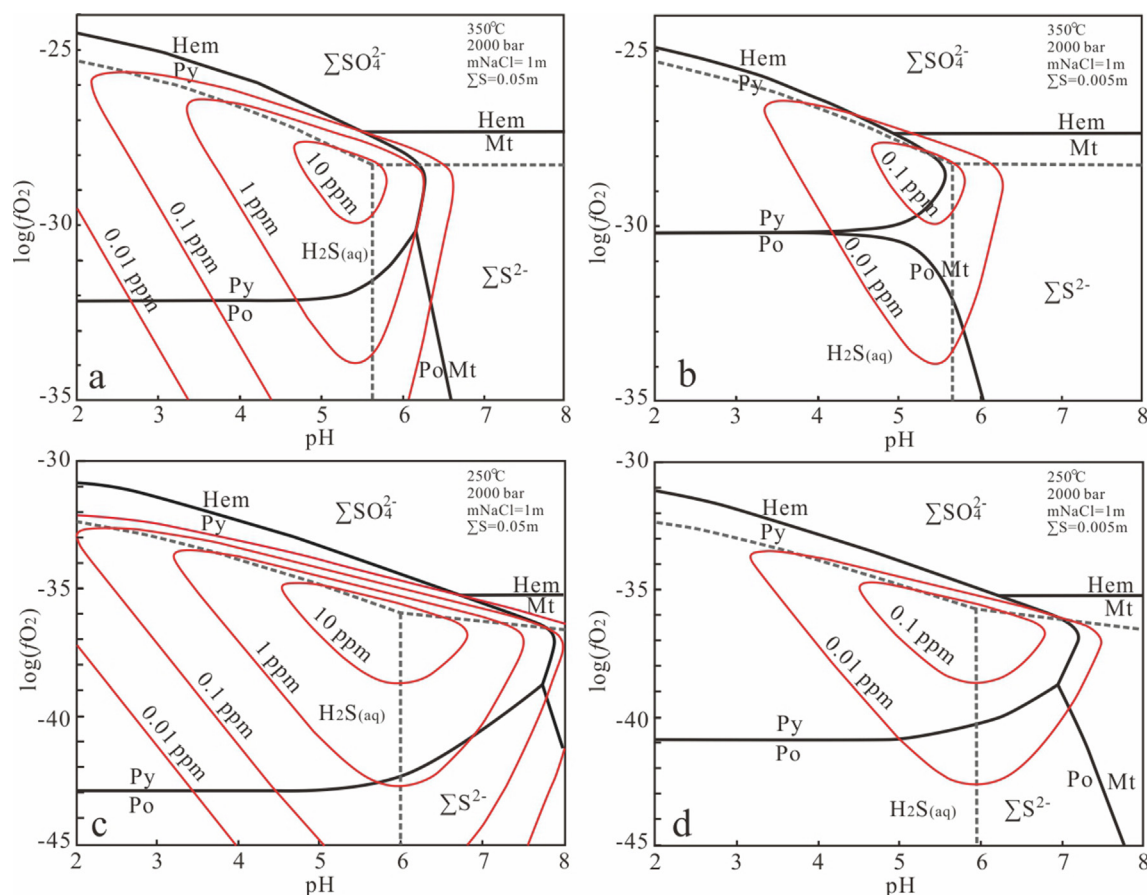

Fig. 14. Thermodynamic modelling on gold solubility as the function of pH, oxygen fugacity (f_{O2}), temperature and $\sum$S in the S-bearing H_2O-NaCl fluids. The modelling follows the methods of Ohmoto (1972), which was conducted by using the software package of *SUPCRT92* (Johnson et al., 1992). The setups of the physicochemical parameters (temperature, pressure, salinity, pH, oxygen fugacity and $\sum$S content) are based on the available results for the ore-forming fluids from the Jiaodong gold deposits (Qiu et al., 2002; Fan et al., 2007; Goldfarb and Santosh, 2014).

show significant vertical change. One possible explanation is that the homogenization temperatures obtained by previous studies were not corrected by pressure, leading to the underestimation of the vertical change of the temperature. On the other hand, it may imply that the Bi concentration in pyrite is more sensitive to temperature, which can be potentially used as an indicator of temperature variation. The wide variations of gold fineness in the shallowest samples from the Linglong deposit could be due to the rapid transportation of the fluids and fluid boiling enhancedly occurring at the shallow settings, where the pH was significantly changed.

6.4. Implications for giant gold mineralization

The generation of giant ore deposits commonly requires optimized conditions, such as abundant supply of ore-forming materials and enhanced ore-forming processes (Richards, 2013; Moncada et al., 2019). Fluid-rock interaction is one of the major ore-forming processes in the hydrothermal gold deposits, which not only leads to the Au deposition (Pokrovski et al., 2014), but also results in the high-grade ores (Petrella et al., 2021). This study shows that, in addition to these effects, fluid-rock interaction can also play a significant role in providing additional Au for the gold mineralization. Hydrothermal fluid leaching Au from wallrocks has been identified in the Carlin-type gold deposits due to the presence of Au- and As-rich sedimentary wallrocks (Cline et al., 2005; Kesler et al., 2005; Emsbo et al., 2006; Large et al., 2011), but is not common in the granite-hosted gold deposits. Our results indicate that Au-rich sequences might be generated during Precambrian metamorphism and stored in the metamorphic terrains, which can be remobilized during later hydrothermal activities through fluid-rock interaction and contribute to the Au mineralization (Fig. 15). The mineralization thus can have nothing to do with the timing of the metamorphism and occur in any type of wallrocks. Since numerous studies concerned with the role of mantle-derived fluids or melts in providing the huge amounts of Au for the Jiaodong gold deposits, it is necessary to emphasize the gold endowment of Precambrian metamorphic rocks.

Pyrite geochemistry and gold fineness vary over time and space, indicating that multiple mechanisms contributed to the Au deposition. The controlling factors causing Au deposition largely depend on the structural settings, where fluid unmixing typically occurred in the extensional settings while fluid-rock interaction occurred in the transpressional settings. This indicates that favorable locations for Au mineralization changed along pathways, which might make finding high-grade ores difficult. The Bi concentrations in pyrite and gold fineness show depth/temperature-dependent variations, implying their potentials for constraining the depth or temperature conditions. In addition, because Bi-Te-S complexes have strong abilities to transport Au and Ag (Cook and Ciobanu, 2004; Ciobanu et al., 2010; Voronin and Osadchii, 2013), the effects of these complexes under high-temperature conditions or in the deep depths should be concerned. The variable ore-forming processes during giant mineralization complicated the elemental and isotopic systems (Fig. 15), alerting us to be cautious when tracing the real origin of the gold.

7. Conclusions

In-situ textural, elemental and isotopic studies on pyrite and electrum reveal the spatiotemporal variations of the ore-forming processes, providing new insights into the sources and mineralization mechanisms of Au.
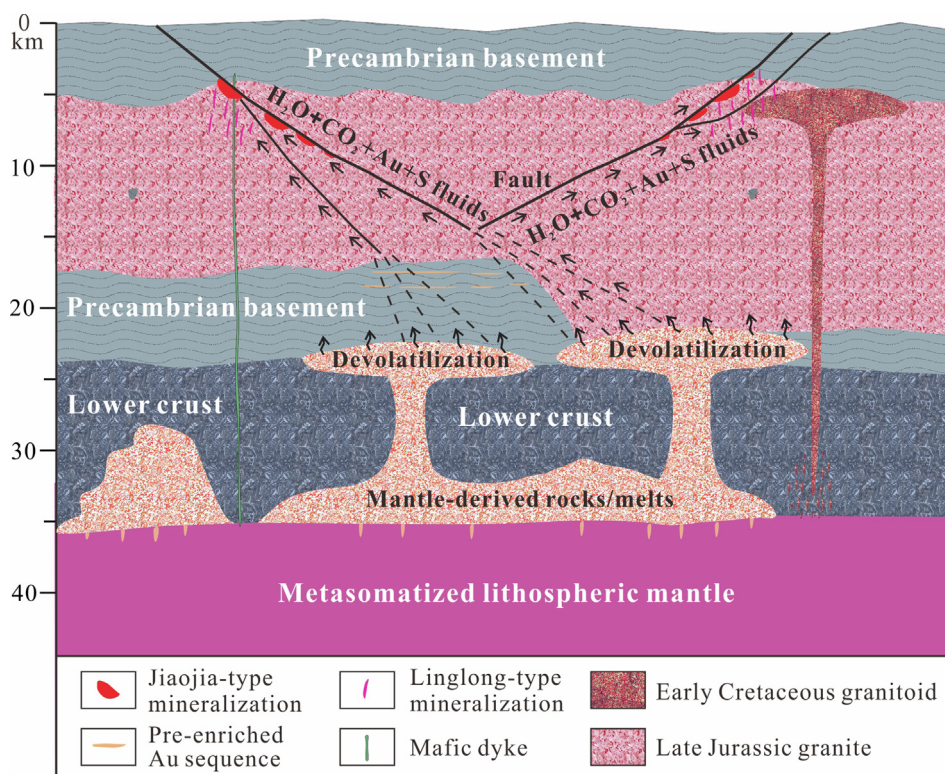

Fig. 15. A schematic model for the generation of the studied gold deposits. The origin of the auriferous fluids is based on Wang et al. (2022). It indicates that the primary auriferous fluids were transported along different faults (pathways), leaching additional ore-forming metals from the preliminarily Au-enriched sequences in the Precambrian basement. The different mineralization styles (Lingong- and Jiaojia-type) were controlled by structural regimes, showing different occurrences and relationships to the major faults.

1. Auriferous fluids reacted with wallrocks along pathways, which not only led to the deposition of Au, but also leached Au from the wallrocks. The Precambrian metasedimentary rocks might play a nonnegligible role in providing additional Au for the giant gold mineralization in the Jiaodong Peninsula.
2. Various mechanisms controlled the remarkable Au deposition. Fluid unmixing typically occurred in the extensional settings while fluid-rock interaction occurred in the transpressional settings, leading to the lode-type and disseminated and stockwork-type mineralization, respectively.
3. Bi concentration in pyrite and gold fineness decrease with shallowing, indicating that cooling affected Au deposition. They might be good indicators for constraining the depth or temperature conditions.
4. Bi-Te-S minerals occurred at the deep depths, suggesting that the original auriferous fluids were enriched in Bi and Te, which might play a significant role in transporting Au and Ag at high-temperature conditions.

Declaration of Competing Interest

The authors declare that they have no known competing financial interests or personal relationships that could have appeared to influence the work reported in this paper.

CRediT authorship contribution statement

Ting-Guang Lan: Investigation, Formal analysis, Writing – original draft. **Hong Wang:** Investigation, Formal analysis. **Hong-Rui Fan:** Supervision, Funding acquisition. **Thomas Ulrich:** Writing – review & editing. **Huan-Long Hu:** Data curation, Visualization. **You-Wei Chen:** Formal analysis, Data curation. **Lei Shu:** Investigation.

Declaration of Competing Interest

The authors declare that they have no known competing financial interests or personal relationships that could have appeared to influence the work reported in this paper.

Acknowledgements

Appendix A. Supplementary data

Supplementary data to this article can be found online at https://doi.org/10.1016/j.gr.2023.02.008.

References

Bao, Z.A., Chen, L., Zong, C.L., Yuan, H.L., Chen, K.Y., Dai, M.L., 2017. Development of pressed sulfide powder tablets for in situ sulfur and lead isotope measurement using LA-MC-ICP-MS. Int. J. Mass Spectrom. 421, 255–262.

Chai, P., Hou, Z.Q., Zhang, Z.Y., 2017. Geology, fluid inclusion and stable isotope constraints on the fluid evolution and resource potential of the Xiadian gold deposit, Jiaodong Peninsula. Resour. Geol. 67, 341–359.

Chang, Z.S., Large, R.R., Maslennikov, V., 2008. Sulfur isotopes in sediment-hosted orogenic gold deposits: evidence for an early timing and a seawater sulfur source. Geology 36, 971–974.

Chen, Y.J., Pirajno, F., Qi, J.P., 2005. Origin of gold metallogeny and sources of ore-forming fluids, Jiaodong Province, Eastern China. Int. Geol. Rev. 47, 530–549.

Ciobanu, C.L., Birch, W.D., Cook, N.J., Pring, A., Grundler, P.V., 2010. Petrogenetic significance of Au-Bi-Te-S associations: The example of Maldon, Central Victorian gold province, Australia. Lithos 116, 1–17.

Cline, J.S., Hofstra, A.H., Muntean, J.L., Tosdal, R.M., Hickey, K.A., 2005. Carlin-type gold deposits in Nevada: Critical geologic characteristics and viable models. Economic Geology 100th Anniversary Volume, 451–484.

Cook, N.J., Ciobanu, C.L., 2004. Bismuth tellurides and sulphosalts from the Larga hydrothermal system, Metaliferi Mts, Romania: Paragenesis and genetic significance. Mineral. Mag. 68, 301–321.

Cook, N.J., Ciobanu, C.L., Wagner, T., Stanley, C.J., 2007. Minerals of the system Bi-Te-Se-S related to the tetradymite archetype: review of classification and compositional variation. Can. Mineral. 45, 665–708.

Cook, N.J., Ciobanu, C.L., Meria, D., Silcock, D., Wade, B., 2013. Arsenopyrite-pyrite association in an orogenic gold ore: Tracing mineralization history from textures and trace elements. Econ. Geol. 108, 1273–1283.

Crossley, R.J., Evans, K.A., Jeon, H., Kilburn, M.R., 2018. Insights into sulfur cycling at subduction zones from in-situ isotopic analysis of sulfides in high-pressure serpentinites and 'hybrid' samples from Alpine Corsica. Chem. Geol. 493, 359–378.

Cui, W., Guo, J., Huang, G., Wang, Z., Liu, Y., Yang, J., 2022. Gold mobilization during prograde metamorphism of clastic sedimentary rocks: An example from the Liaohe Group in the Jiao–Liao–Ji Belt. North China Craton. Ore Geology Reviews 140, 104624.

Danyushevsky, L., Robinson, P., Gilbert, S., Norman, M., Large, R., McGoldrick, P., Shelley, M., 2011. Routine quantitative multi-element analysis of sulphide minerals by laser ablation ICP-MS: Standard development and consideration of matrix effects. Geochemistry: Exploration. Environment, Analysis 11, 51–60.

Deng, J., Liu, X., Wang, Q., Dilek, Y., Liang, Y., 2017. Isotopic characterization and petrogenetic modeling of Early Cretaceous mafic diking-Lithospheric extension in the North China craton, eastern Asia. Geol. Soc. Am. Bull. 129, 1379–1407.

Deng, J., Yang, L.Q., Li, R.H., Groves, D.I., Santosh, M., Wang, Z.L., Sai, S.X., Wang, S.R., 2019. Regional structural control on the distribution of world-class gold deposits: An overview from the Giant Jiaodong Gold Province, China. Geol. J. 54, 378–391.

Deng, J., Wang, Q.F., Santosh, M., Liu, X.F., Liang, Y.Y., Zhao, R., Yang, L., 2020a. Remobilization of metasomatized mantle lithosphere: a new model for the Jiaodong gold province, eastern China. Miner. Deposita 55, 257–274.

Deng, J., Yang, L.Q., Groves, D.I., Zhang, L., Qiu, K.F., Wang, Q.F., 2020b. An integrated mineral system model for the gold deposits of the giant Jiaodong province, eastern China. Earth-Science Review 208, 103274.

Drummond, S.E., Ohmoto, H., 1985. Chemical evolution and mineral deposition in boiling hydrothermal systems. Econ. Geol. 80, 126–147.

Emsbo, P., Groves, D.I., Hofstra, A.H., Bierlein, F.P., 2006. The giant Carlin gold province: a protracted interplay of orogenic, basinal, and hydrothermal processes above a lithospheric boundary. Miner. Deposita 41, 517–525.

Evans, K.A., Tomkins, A.G., Cliff, J., Fiorentini, M.L., 2014. Insights into subduction zone sulfur recycling from isotopic analysis of eclogite-hosted sulfides. Chem. Geol. 365, 1–19.

Fan, H.R., Hu, F.F., Yang, J.H., Zhai, M.G., 2007. Fluid evolution and large-scale gold metallogeny during Mesozoic tectonic transition in the Jiaodong Peninsula, eastern China. Geol. Soc. Lond. Spec. Publ. 280, 303–316.

Fan, H., Lan, T., Li, X., Santosh, M., Yang, K., Fan, F., Feng, K., Hu, H., Peng, H., Zhang, Y., 2021. Conditions and processes leading to large-scale gold deposition in the Jiaodong province, eastern China. Sci. China Earth Sci. 64, 1504–1523.

Farquhar, J., Wu, N., Canfield, D.E., Oduro, H., 2010. Connections between sulfur cycle evolution, sulfur isotopes, sediments, and base metal sulfide deposits. Econ. Geol. 105, 509–533.

Feng, K., Fan, H.R., Groves, D.I., Yang, K.F., Hu, F.F., Li, X., Cai, Y.C., 2020. Geochronological and sulfur isotopic evidence for the genesis of the post-magmatic, deeply sourced, and anomalously gold-rich Daliuhang orogenic deposit, Jiaodong, China. Miner. Deposita 55, 293–308.

Fougerouse, D., Micklethwaite, S., Tomkins, A.G., Mei, Y., Kilburn, M., Guagliardo, P., Fisher, L.A., Halfpenny, A., Gee, M., Paterson, D., Howard, D.L., 2016. Gold remobilisation and formation of high grade ore shoots driven by dissolution-reprecipitation replacement and Ni substitution into auriferous arsenopyrite. Geochim. Cosmochim. Acta 178, 143–159.

Gammons, C.H., Williams-Jones, A.E., 1995. Hydrothermal geochemistry of electrum: thermodynamic constraints. Econ. Geol. 90, 420–432.

Gartman, A., Hannington, M., Jamieson, J.W., Peterkin, B., Garbe-Schönberg, D., Findlay, A.J., Fuchs, S., Kwasnitschka, T., 2018. Boiling-induced formation of colloidal gold in black smoker hydrothermal fluids. Geology 46, 39–42.

Goldfarb, R.J., Santosh, M., 2014. The dilemma of the Jiaodong gold deposits: Are they unique? Geosci. Front. 5, 139–153.

Goss, S.C., Wilde, S.A., Wu, F., Yang, J., 2010. The age, isotopic signature and significance of the youngest Mesozoic granitoids in the Jiaodong Terrane, Shandong Province, North China Craton. Lithos 120, 309–326.

Groves, D.I., Santosh, M., 2016. The giant Jiaodong gold province: The key to a unified model for orogenic gold deposits? Geosci. Front. 7, 409–417.

Groves, D.I., Goldfarb, R.J., Santosh, M., 2016. The conjunction of factors that lead to formation of giant gold provinces and deposits in non-arc settings. Geosci. Front. 7, 303–314.

Guo, L.N., Goldfarb, R.J., Wang, Z.L., Li, R.H., Chen, B.H., Li, J.L., 2017. A comparison of Jiaojia- and Linglong-type gold deposit ore-forming fluids: Do they differ? Ore Geol. Rev. 88, 511–533.

Guo, L.N., Deng, J., Yang, L.Q., Wang, Z.L., Wang, S.R., Wei, Y.J., Chen, B.H., 2020. Gold deposition and resource potential of the Linglong gold deposit, Jiaodong Peninsula, Geochemical comparison of ore fluids. Ore Geol. Rev. 120, 103434.

Hastie, E.C.G., Schindler, M., Kontak, D.J., Lafrance, B., 2021. Transport and coarsening of gold nanoparticles in an orogenic deposit by dissolution–reprecipitation and Ostwald ripening. Communications Earth & Environment 2, 57.

Hu, H.L., Fan, H.R., Liu, X., Cai, Y.C., Yang, K.F., Ma, W.D., 2020a. Two-stage gold deposition in response to H_2S loss from a single fluid in the Sizhuang deposit, Jiaodong. China. Ore Geology Reviews 120, 103450.

Hu, H.L., Fan, H.R., Santosh, M., Liu, X., Cai, Y.C., Yang, K.F., 2020b. Ore-forming processes in the Wang'ershan gold deposit, Jiaodong, China: Insight from microtexture, mineral chemistry and sulfur isotope compositions. Ore Geol. Rev. 123, 103600.

Hu, H.L., Fan, H.R., Lan, T.G., Xu, Y., Cai, Y.C., Yang, K.F., Dai, Z.H., 2022. New constraints for crustal sulfur contamination of gold source: Evidence from complex $\delta^{34}S$ of pyrite in the northwestern Jiaodong gold province. China. Precambrian Research 378, 106773.

Hutchison, W., Finch, A.A., Boyce, A.J., 2020. The sulfur isotope evolution of magmatic-hydrothermal fluids: insights into ore-forming processes. Geochim. Cosmochim. Acta 288, 176–198.

Jahn, B.M., Liu, D., Wan, Y., Song, B., Wu, J., 2008. Archean crustal evolution of the Jiaodong Peninsula, China, as revealed by zircon SHRIMP geochronology, elemental and Nd-isotope geochemistry. Am. J. Sci. 308, 232–269.

Johnson, J.W., Oelkers, E.H., Helgeson, H.C., 1992. SUPCRT92: A software package for calculating the standard molal thermodynamic properties of minerals, gases, aqueous species, and reactions from 1 to 5000 bar and 0 to 1000 °C. Comput. Geosci. 18, 899–947.

Kesler, S.E., Riciputi, L.C., Ye, Z., 2005. Evidence for a magmatic origin for Carlin-type gold deposits: isotopic composition of sulfur in the Betze-Post-Screamer Deposit, Nevada, USA. Miner. Deposita 40, 127–136.

Kokh, M.A., Akinfiev, N.N., Pokrovski, G.S., Salvi, S., Guillaume, D., 2017. The role of carbon dioxide in the transport and fractionation of metals by geological fluids. Geochim. Cosmochim. Acta 197, 433–466.

Large, R.R., Bull, S.W., Maslennikov, V.V., 2011. A carbonaceous sedimentary source-rock model for Carlin-type and orogenic gold deposits. Econ. Geol. 106, 331–358.

Li, D., Duan, Z., 2007. The speciation equilibrium coupling with phase equilibrium in the $H_2O–CO_2–NaCl$ system from 0 to 250 °C, from 0 to 1000 bar, and from 0 to 5 molality of NaCl. Chem. Geol. 244, 730–751.

Li, X.H., Fan, H.R., Yang, K.F., Hollings, P., Liu, X., Hu, F.F., Cai, Y.C., 2018. Pyrite textures and compositions from the Zhuangzi Au deposit, southeastern North China Craton: implication for ore-forming processes. Contrib. Miner. Petrol. 173, 73.

Li, L., Santosh, M., Li, S.R., 2015. The "Jiaodong type" gold deposits: Characteristics, origin and prospecting. Ore Geol. Rev. 65, 589–611.

Li, L., Li, S.R., Santosh, M., Li, Q., Gu, Y., Lü, W.J., Zhang, H.F., Shen, J.F., Zhao, G.C., 2016. Dyke swarms and their role in the genesis of world-class gold deposits: Insights from the Jiaodong peninsula, China. J. Asian Earth Sci. 130, 2–22.

Li, S.R., Santosh, M., 2014. Metallogeny and craton destruction: Records from the North China Craton. Ore Geol. Rev. 56, 376–414.

Li, Q., Song, H., Chi, G., Zhang, G., Xu, Z., 2021. Genesis of visible gold in pyrite in the Zhaoxian gold deposit, Jiaodong gold province, China: Constraints from EBSD micro-structural and LA-ICP-MS elemental analyses. Ore Geol. Rev. 139, 104591.

Liang, Y., Hoshino, K., 2015. Thermodynamic calculations of $Au_xAg_{1−x}$–Fluid equilibria and their applications for ore-forming conditions. Appl. Geochem. 52, 109–117.

Ling, W., Xie, X., Liu, X., Cheng, J., 2007. Zircon U-Pb dating on the Mesozoic volcanic suite from the Qingshan Group stratotype section in eastern Shandong Province and its tectonic significance. Sci. China. Ser. D Earth Sci. 50, 813–824.

Liu, Z., Hollings, P., Mao, X., Lawley, C.J.M., Yang, B., Tang, L., 2021. Metal remobilization from country rocks into the Jiaodong-type orogenic gold systems, Eastern China: New constraints from scheelite and galena isotope results at the Xiadian and Majiayao gold deposits. Ore Geol. Rev. 104126.

Liu, J., Wang, J., Liu, Y., Tian, J., Li, X., Zhang, H., 2018. Ore genesis of the Xiadian gold deposit, Jiaodong Peninsula, East China: Information from fluid inclusions and mineralization. Geol. J. 53, 77–95.

Ma, W.D., Fan, H.R., Liu, X., Yang, K.F., Hu, F.F., Zhao, K., Cai, Y.C., Hu, H.L., 2018. Hydrothermal fluid evolution of the Jintingling gold deposit in the Jiaodong peninsula, China: Constraints from U-Pb age, CL imaging, fluid inclusion and stable isotope. J. Asian Earth Sci. 160, 287–303.

Mao, J., Wang, Y., Li, H., Pirajno, F., Zhang, C., Wang, R., 2008. The relationship of mantle-derived fluids to gold metallogenesis in the Jiaodong Peninsula: Evidence from D-O-C-S isotope systematics. Ore Geol. Rev. 33, 361–381.

McLeish, D.F., Williams-Jones, A.E., Vasyukova, O.V., Clark, J.R., Boar,d W.S., 2021. Colloidal transport and flocculation are the cause of the hyperenrichment of gold in nature. Proceedings of the National Academy of Sciences 118, e2100689118.

Mikucki, E.J., 1998. Hydrothermal transport and depositional processes in Archean lode-gold systems: A review. Ore Geol. Rev. 13, 307–321.

Mills, S.E., Tomkins, A.G., Weinberg, R.F., Fan, H.R., 2015. Anomalously silver-rich vein-hosted mineralisation in disseminated-style gold deposits, Jiaodong gold district, China. Ore Geol. Rev. 68, 127–141.

Moncada, D., Rimstidt, J.D., Bodnar, R.J., 2019. How to form a giant epithermal precious metal deposit: Relationships between fluid flow rate, metal concentration of ore-forming fluids, duration of the ore-forming process, and ore grade and tonnage. Ore Geol. Rev. 113, 103066.

Morey, A.A., Tomkins, A.G., Bierlein, F.P., Weinberg, R.F., Davidson, G.J., 2008. Bimodal distribution of gold in pyrite and arsenopyrite: examples from the Archean Boorara and Bardoc shear systems, Yilgarn Craton, Western Australia. Econ. Geol. 103, 599–614.

Ohmoto, H., 1972. Systematics of sulfur and carbon isotopes in hydrothermal ore deposits. Econ. Geol. 67, 551–578.

Pal'yanova, G., 2008. Physicochemical modeling of the coupled behavior of gold and silver in hydrothermal processes: Gold fineness, Au/Ag ratios and their possible implications. Chem. Geol. 255, 399–413.

Paton, C., Hellstrom, J., Paul, B., Woodhead, J., Hergt, J., 2011. Iolite: Freeware for the visualisation and processing of mass spectrometric data. J. Anal. At. Spectrom 26, 2508–2518.

Peng, H.W., Fan, H.R., Liu, X., Wen, B.J., Zhang, Y.W., Feng, K., 2021. New insights into the control of visible gold fineness and deposition: A case study of the Sanshandao gold deposit, Jiaodong, China. Am. Mineral. 106, 135–149.

Peterson, E.C., Mavrogenes, J.A., 2014. Linking high-grade gold mineralization to earthquake-induced fault-valve processes in the Porgera gold deposit, Papua New Guinea. Geology 42, 383–386.

Petrella, L., Thébaud, N., Evans, K., LaFlamme, C., Occhipinti, S., 2021. The role of competitive fluid-rock interaction processes in the formation of high-grade gold deposits. Geochim. Cosmochim. Acta 313, 38–54.

Pokrovski, G.S., Roux, J., Ferlat, G., Jonchiere, R., Seitsonen, A.P., Vuilleumier, R., Hazemann, J.L., 2013. Silver in geological fluids from in situ X-ray absorption spectroscopy and first principles molecular dynamics. Geochim. Cosmochim. Acta 106, 501–523.

Pokrovski, G.S., Akinfiev, N.N., Borisova, A.Y., Zotov, A.V., Kouzmanov, K., 2014. Gold speciation and transport in geological fluids: insights from experiments and physical-chemical modelling. Geol. Soc. Lond. Spec. Publ. 402, 9–70.

Qiu, Y.M., Groves, D.I., McNaughton, N.J., Wang, L.J., Zhou, T., 2002. Nature, age and tectonic setting of granitoid-hosted orogenic gold deposits of the Jiaodong Peninsula, eastern North China craton, China. Miner. Deposita 37, 283–305.

Ramboz, C., Pichavant, M., Weisbrod, A., 1982. Fluid immiscibility in natural processes: Use and misuse of fluid inclusion data: II Interpretation of fluid inclusion data in terms of immiscibility. Chem. Geol. 37, 29–48.

Reed, M.H., Palandri, J., 2006. Sulfide mineral precipitation from hydrothermal fluids. Rev. Mineral. Geochem. 61, 609–631.

Richards, J.P., 2013. Giant ore deposits formed by optimal alignments and combinations of geological processes. Nat. Geosci. 6, 911–916.

Saunders, J., Burke, M., 2017. Formation and aggregation of gold (electrum) nanoparticles in epithermal ores. Minerals 7, 163.

Simmons, S.F., Brown, K.L., 2006. Gold in magmatic hydrothermal solutions and the rapid formation of a giant ore deposit. Science 314, 288–291.

Song, M.C., Li, S.Z., Santosh, M., Zhao, S., Yu, S., Yi, P.H., Cui, S.X., Lv, G.X., Xu, J.X., Song, Y.X., Zhou, M.L., 2015. Types, characteristics and metallogenesis of gold deposits in the Jiaodong Peninsula, Eastern North China Craton. Ore Geol. Rev. 65, 612–625.

Tan, J., Wei, J., He, H., Su, F., Li, Y., Fu, L., Zhao, S., Xiao, G., Zhang, F., Xu, J., Liu, Y., Stuart, F.M., Zhu, R., 2018. Noble gases in pyrites from the Guocheng-Liaoshang gold belt in the Jiaodong province: Evidence for a mantle source of gold. Chem. Geol. 480, 105–115.

Tooth, B., Etschmann, B., Pokrovski, G.S., Testemale, D., Hazemann, J.L., Grundler, P. V., Brugger, J., 2013. Bismuth speciation in hydrothermal fluids: An X-ray absorption spectroscopy and solubility study. Geochim. Cosmochim. Acta 101, 156–172.

Trigub, A.L., Tagirov, B.R., Kvashnina, K.O., Lafuerza, S., Filimonova, O.N., Nickolsky, M.S., 2017. Experimental determination of gold speciation in sulfide-rich hydrothermal fluids under a wide range of redox conditions. Chem. Geol. 471, 52–64.

Ulrich, T., Kamber, B.S., Jugo, P.J., Tinkham, D.K., 2009. Imaging element distribution patterns in minerals by laser ablation-inductively coupled plasma-mass spectrometry (LA-ICP-MS). Can. Mineral. 47, 1001–1012.

Voronin, M.V., Osadchii, E.G., 2013. Thermodynamic properties of silver and bismuth sulfosalt minerals, pavonite ($AgBi_3S_5$) and matildite ($AgBiS_2$) and implications for ore deposits. Econ. Geol. 108, 1203–1210.

Wan, Y., Song, B., Liu, D., Wilde, S.A., Wu, J., Shi, Y., Yin, X., Zhou, H., 2006. SHRIMP U-Pb zircon geochronology of Palaeoproterozoic metasedimentary rocks in the North China Craton: Evidence for a major Late Palaeoproterozoic tectonothermal event. Precambr. Res. 149, 249–271.

Wang, H., Chen, J., Wang, Y., Ding, K., 1989. Geochemical studies of Au-bearing formation in Jiaodong Peninsula, Shandong province. Chin. J. Geochem. 8, 213–227.

Wang, Z.C., Cheng, H., Zong, K.Q., Geng, X.L., Liu, Y.S., Yang, J.H., Wu, F.Y., Becker, H., Foley, S., Wang, C.Y., 2020. Metasomatized lithospheric mantle for Mesozoic giant gold deposits in the North China craton. Geology 48, 169–173.

Wang, H., Lan, T.G., Fan, H.R., Huan, Z.L., Hu, H.L., Chen, Y.H., Tang, Y.W., Li, J., 2022. Fluid origin and critical ore-forming processes for the giant gold mineralization in the Jiaodong Peninsula, China: Constraints from in situ elemental and oxygen isotopic compositions of quartz and LA-ICP-MS analysis of fluid inclusions. Chem. Geol. 608, 121027.

Wang, Z., Xu, Z., Cheng, H., Zou, Y., Guo, J., Liu, Y., Yang, J., Zong, K., Xiong, L., Hu, Z., 2021. Precambrian metamorphic crustal basement cannot provide much gold to form giant gold deposits in the Jiaodong Peninsula. China. Precambrian Research 354, 106045.

Ward, J., Mavrogenes, J., Murray, A., Holden, P., 2017. Trace element and sulfur isotopic evidence for redox changes during formation of the Wallaby Gold Deposit, Western Australia. Ore Geol. Rev. 82, 31–48.

Wen, B.J., Fan, H.R., Santosh, M., Hu, F.F., Pirajno, F., Yang, K.F., 2015. Genesis of two different types of gold mineralization in the Linglong gold field, China: Constrains from geology, fluid inclusions and stable isotope. Ore Geol. Rev. 65, 643–658.

Wen, B.J., Fan, H.R., Hu, F.F., Liu, X., Yang, K.F., Sun, Z.F., Sun, Z.F., 2016. Fluid evolution and ore genesis of the giant Sanshandao gold deposit, Jiaodong gold province, China: Constrains from geology, fluid inclusions and H-O-S-He-Ar isotopic compositions. J. Geochem. Explor. 171, 96–112.

Wilkinson, J.J., Stoffell, B., Wilkinson, C.C., Jeffries, T.E., Appold, M.S., 2009. Anomalously metal-rich fluids form hydrothermal ore deposits. Science 323, 764–767.

Williams-Jones, A.E., Bowell, R.J., Migdisov, A.A., 2009. Gold in solution. Elements 5, 281–287.

Wilson, S.A., Ridley, W.I., Koenig, A.E., 2002. Development of sulfide calibration standards for the laser ablation inductively-coupled plasma mass spectrometry technique. J. Anal. At. Spectrom 17, 406–409.

Wu, Y.B., Zheng, Y.F., 2013. Tectonic evolution of a composite collision orogeny: An overview on the Qinling-Tongbai-Hong'an-Dabie-Sulu orogenic belt in central China. Gondw. Res. 23, 1402–1428.

Xiong, L., Zhao, X., Zhao, S., Lin, H., Lin, Z., Zhu, Z., Wang, Z., Li, M.Y.H., Li, J., 2021. Formation of giant gold provinces by subduction-induced reactivation of fossilized, metasomatized continental lithospheric mantle in the North China Craton. Chem. Geol. 580, 120362.

Xu, H., 1998. Genesis and geological and geochemical characteristics of Qixia gold deposit, Shandong, China. Chin. J. Geochem. 17, 338–345.

Xu, W., Liu, F., 2019. Geochronological and geochemical insights into the tectonic evolution of the Paleoproterozoic Jiao-Liao-Ji Belt, Sino-Korean Craton. Earth Sci. Rev. 193, 162–198.

Yan, Y., Zhang, N., Li, S., Li, Y., 2014. Mineral chemistry and isotope geochemistry of pyrite from the Heilangou gold deposit, Jiaodong Peninsula, Eastern China. Geosci. Front. 5, 205–213.

Yang, J.H., Chung, S.L., Wilde, S.A., Wu, F.Y., Chu, M.F., Lo, C.H., Fan, H.R., 2005. Petrogenesis of post-orogenic syenites in the Sulu Orogenic Belt, East China: geochronological, geochemical and Nd-Sr isotopic evidence. Chem. Geol. 214, 99–125.

Yang, L.Q., Deng, J., Wang, Z.L., Guo, L.N., Li, R.H., Groves, D.I., Danyushevsky, L.V., Zhang, C., Zheng, X.L., Zhao, H., 2016a. Relationships between gold and pyrite at the Xincheng gold deposit, Jiaodong Peninsula, China: Implications for gold source and deposition in a brittle epizonal environment. Econ. Geol. 111, 105–126.

Yang, L.Q., Deng, J., Guo, L.N., Wang, Z.L., Li, X.Z., Li, J.L., 2016b. Origin and evolution of ore fluid, and gold-deposition processes at the giant Taishang gold deposit, Jiaodong Peninsula, eastern China. Ore Geol. Rev. 72, 585–602.

Yang, K.F., Fan, H.R., Santosh, M., Hu, F.F., Wilde, S.A., Lan, T.G., Lu, L.N., Liu, Y.S., 2012. Reactivation of the Archean lower crust: Implications for zircon geochronology, elemental and Sr-Nd-Hf isotopic geochemistry of late Mesozoic granitoids from northwestern Jiaodong Terrane, the North China Craton. Lithos 146, 112–127.

Yang, K.F., Jiang, P., Fan, H.R., Zuo, Y.B., Yang, Y.H., 2018. Tectonic transition from a compressional to extensional metallogenic environment at ~120 Ma revealed in the Hushan gold deposit, Jiaodong, North China Craton. J. Asian Earth Sci. 160, 408–425.

Yuan, Z.Z., Li, Z.K., Zhao, X.F., Sun, H.S., Qiu, H.N., Li, J.W., 2019. New constraints on the genesis of the giant Dayingezhuang gold, silver. deposit in the Jiaodong district, North China Craton. Ore Geology Reviews 112, 103038.

Yuan, Z.Z., Li, Z.K., Li, J.W., Zhao, X.F., Wu, Y.F., Hu, H.J., Sun, H.S., 2021. Occurrence and remobilization of gold in the Dayingezhuang deposit in Jiaodong, North China Craton: Evidence from textural and geochemical features of pyrite. Ore Geol. Rev. 136, 104243.

Yuan, J.H., Zhan, X.C., Fan, C.Z., Zhao, L.H., Sun, D.Y., Jia, Z.R., Hu, M.Y., Kuai, L.J., 2012. Quantitative analysis of sulfide minerals by laser ablation-inductively coupled plasma-mass spectrometry using glass reference materials with matrix normalization plus sulfur internal standardization calibration. Chin. J. Anal. Chem. 40, 201–207.

Zhang, L., Weinberg, R.F., Yang, L.Q., Groves, D.I., Sai, S.X., Matchan, E., Phillips, D., Kohn, B.P., Miggins, D.P., Liu, Y., Deng, J., 2020. Mesozoic orogenic gold mineralization in the Jiaodong Peninsula, China: A focused event at 120±2 Ma during cooling of pregold granite intrusions. Econ. Geol. 115, 415–441.

Zhu, G., Lu, Y., Su, N., Wu, X., Yin, H., Zhang, S., Xie, C., Niu, M., 2021. Crustal deformation and dynamics of Early Cretaceous in the North China Craton. Sci. China Earth Sci. 64, 1428–1450.

Zhu, R., Sun, W., 2021. The big mantle wedge and decratonic gold deposits. Sci. China Earth Sci. 64, 1451–1462.